Electronic Supplementary Material (ESI) for Journal of Materials Chemistry C.
This journal is © The Royal Society of Chemistry 2021

ELECTRONIC SUPPLEMENTARY INFORMATION

Easy-Plane to Easy-Axis Anisotropy Switching in a Co(II) Single-Ion Magnet Triggered by Diamagnetic Lattice

Joscha Nehrkorn,[‡a,b,c,d] Igor A. Valuev,[‡e,f] Mikhail A. Kiskin,[g] Artem S. Bogomyakov,[e,f] Elizaveta A. Suturina,[f,h] Alena M. Sheveleva,[e,f] Victor I. Ovcharenko,[e] Karsten Holldack,[a] Carmen Herrmann,[c] Matvey V. Fedin,[e,f] Alexander Schnegg[a,d,*] and Sergey L. Veber[e,f,*]

a. Helmholtz-Zentrum Berlin für Materialien und Energie, Berlin, Germany
b. Department of Chemistry, University of Washington, Seattle, WA, United States
c. Institut für Anorganische und Angewandte Chemie, Universität Hamburg, Hamburg, Germany
d. Max Planck Institute for Chemical Energy Conversion, Mülheim/Ruhr, Germany
e. International Tomography Center SB RAS, Novosibirsk, Russia
f. Novosibirsk State University, Novosibirsk, Russia
g. N.S. Kurnakov Institute of General and Inorganic Chemistry, Moscow, Russia
h. Department of Chemistry, University of Bath, Claverton Down, Bath, BA2 7AY, UK
‡ These authors contributed equally.
*e-mail: sergey.veber@tomo.nsc.ru, alexander.schnegg@cec.mpg.de

Table of Content

1. Synthesis and analysis

The compounds were synthesized on air, the commercially available acetonitrile (99%) and 2-amino-pyridine (2-NH_2-Py, 99%) were used without further purification. Compounds $[Zn(Piv)_2]_n$ and $[Co(Piv)_2]_n$ were prepared according to the literature procedures.[1] Complex $[Co(Piv)_2((2\text{-}NH_2)C_5H_4N)_2]$ was prepared according to the literature procedure.[2]

The series of complexes $[Co_xZn_{(1-x)}(piv)_2(2\text{-}NH_2\text{-}Py)_2]$ (x = 0.9 0.75, 0.5, 0.25, 0.1, 0.03, 0.01) was obtained in one way. Mixture of $[Co(Piv)_2]_n$ and $[Zn(Piv)_2]_n$ was added to the solution of 2-amino-pyridine in MeCN (weight and amount of samples and solvent volume are given in the Table S1). The reaction mixture was stirred for 20-30 min at 80 °C, resulting in the formation of a blue/violet/pale violet/colorless solution. The resulting solution was kept at room temperature for 3 days. Crystals suitable for X-ray diffraction were separated from the mother liquor by decantation, washed with cold MeCN (–5°C), and dried in air at 20 °C.

*Table S 1. Details of synthesis and analysis for $[Co_xZn_{(1-x)}(piv)_2(2\text{-}NH_2\text{-}Py)_2]$ (**1**$_x$, x = 0.9 0.75, 0.5, 0.25, 0.1, 0.03, 0.01).*

Complex	Weight (g) / amount (mmol)			MeCN (mL)	Yield (%)	Crystal color	Elemental analysis, exp / calc	Molar ratio Co : Zn (EDX analysis)
	$[Co(Piv)_2]_n$	$[Zn(Piv)_2]_n$	2-NH_2-Py					
1$_{0.9}$	0.3 / 1.149	0.034 / 0.127	0.24 / 2.55	30	~50	blue	C: 53.5 / 53.4 H: 6.6 / 6.7 N: 12.5 / 12.5	0.028±0.0014 : 0.003±0.0005 = 9.3 referred to as 9 : 1
1$_{0.75}$	0.232 / 0.888	0.102 / 0.381	0.24 / 2.55	30	~50	blue	C: 53.2 / 53.3 H: 6.7 / 6.7 N: 12.3 / 12.4	0.034±0.0017 : 0.011±0.0009 = 3.11 referred to as 3 : 1
1$_{0.5}$	0.165 / 0.632	0.170 / 0.635	0.24 / 2.55	30	~50	violet	C: 53.1 / 53.1 H: 6.7 / 6.7 N: 12.3 / 12.4	0.020±0,001 : 0.019±0.001 = 1.05 referred to as 1 : 1
1$_{0.25}$	0.1 / 0.383	0.24 / 0.897	0.24 / 2.55	30	~60	violet	C: 53.0 / 52.9 H: 6.5 / 6.6 N: 12.4 / 12.3	0.011±0.0008 : 0.028±0.0014 = 0.39 referred to as 1 : 3
1$_{0.1}$	0.025 / 0.0957	0.231 / 0.863	0.18 / 1.91	25	~60	pale violet	C: 52.9 / 52.8 H: 6.7 / 6.6 N: 12.4 / 12.3	0.003±0.0008 : 0.032±0.0016 = 0.09 referred to as 1 : 9
1$_{0.03}$	0.009 / 0.034	0.3 / 1.12	0.218 / 2.32	30	~70	pale violet	C: 52.7 / 52.7 H: 6.6 / 6.6 N: 12.2 / 12.3	-
1$_{0.01}$	0.03 / 0.011	0.3 / 1.12	0.215 / 2.28	30	~70	pale violet	C: 52.6 / 52.7 H: 6.6 / 6.6	-

							N: 12.4 / 12.3	
1_0	-	0.1 / 0.38	0.072 / 0.77	15	~70	colorless	C: 52.6 / 52.7 H: 6.6 / 6.6 N: 12.3 / 12.3	-

1.1. X-ray data tables and PXRD data

Single crystals of compounds were obtained from mother liquor. The X-ray data sets for $[Co_xZn_{(1-x)}(piv)_2(2\text{-}NH_2\text{-}Py)_2]$ with x = 0.9, 0.75, 0.5, 0.25, 0.1 and 0 were collected on a Bruker APEX II diffractometer equipped with a CCD camera and a graphite-monochromated Mo-K_α radiation source (λ = 0.71073 Å).[3] For compounds $[Co_xZn_{(1-x)}(piv)_2(2\text{-}NH_2\text{-}Py)_2]$ (x = 0.25, 0.1 and 0) semi-empirical absorption correction was applied.[4] The structures were solved by direct methods and by Fourier techniques and were refined by the full-matrix least squares method against F^2 with anisotropic thermal parameters for all non-hydrogen atoms. The hydrogen atoms of the carbon-containing ligands in the compounds were positioned geometrically and refined using the riding model. All calculations were carried out with the use of the SHELXL-2014 software packages.[5] CCDC 1914493-1914498 (for $[Co_xZn_{(1-x)}(piv)_2(2\text{-}NH_2\text{-}Py)_2]$ with x = 0.9, 0.75, 0.5, 0.25, 0.1 and 0 respectively) contains the supplementary crystallographic data for this paper. These data can be obtained free of charge from The Cambridge Crystallographic Data Centre. The crystallographic parameters and the refinement statistics are given in Table S 2.

XRPD data of samples were collected using a Bruker D8 Advance diffractometer (CuK_α, λ = 1.54 Å, Ni-filter, LYNXEYE detector, geometry reflection) at RT.

Table S 2 Crystallographic parameters and structure refinement statistics for ***1****$_x$ with x = 1, 0.9, 0.75, 0.5, 0.25, 0.1 and 0.*

Parameters	**1$_1$**	**1$_{0.9}$**	**1$_{0.75}$**	**1$_{0.5}$**	**1$_{0.25}$**	**1$_{0.1}$**	**1$_0$**
CCDC	625391	1914497	1914494	1914495	1914496	1914493	1914498
Ref.	[2]	This work					
Empirical formula	$CoC_{20}H_{30}N_4O_4$	$Co_{0.9}Zn_{0.1}C_{20}H_{30}N_4O_4$	$Co_{0.75}Zn_{0.25}C_{20}H_{30}N_4O_4$	$Co_{0.5}Zn_{0.5}C_{20}H_{30}N_4O_4$	$Co_{0.25}Zn_{0.75}C_{20}H_{30}N_4O_4$	$Co_{0.1}Zn_{0.9}C_{20}H_{30}N_4O_4$	$ZnC_{20}H_{30}N_4O_4$
Formula weight ($g \cdot mol^{-1}$)	449.41	450.05	451.02	452.63	454.24	455.20	455.85
T (K)	100(2)	150(2)	150(2)	150(2)	150(2)	296(2)	150(2)
Crystal system	Monoclinic						
Space group	$P2_1/c$						
a (Å)	11.2306(5)	11.2471(10)	11.2611(9)	11.2630(19)	11.7904(5)	11.9572(10)	11.7525(7)
b (Å)	23.6445(7)	23.713(2)	23.7458(18)	23.767(4)	15.0865(6)	15.2563(13)	15.1377(9)
c (Å)	8.5436(4)	8.5650(7)	8.5582(6)	8.5542(14)	14.2619(6)	14.2673(13)	14.2554(9)
B (deg.)	102.668(4)	102.580(2)	102.5270(10)	102.451(3)	114.1650(10)	113.225(5)	114.1370(10)
V ($Å^3$)	2213.46(16)	2229.5(3)	2234.0(3)	2236.0(6)	2314.54(17)	2391.8(4)	2314.4(2)
Z	4	4	4	4	4	4	4

D_{calc} (g·cm^{-3})	1.349	1.341	1.341	1.345	1.304	1.264	1.308
μ (mm^{-1})	0.807	0.835	0.883	0.965	1.012	1.026	1.092
R_{int}	0.0637	0.0729	0.0813	0.1037	0.0277	0.0340	0.0211
T_{min} / T_{max}	0.284 / 0.325	-	-	-	0.593 / 0.745	0.629 / 0.746	0.659 / 0.746
θ_{max}	25.30	29.47	26.02	25.02	28.28	29.61	28.27
no. of reflns	12893	18439	15491	14729	19571	20964	15079
no. of reflns ($I > 2\sigma(I)$)	2798	4019	2706	2306	4546	4207	4625
GooF	1.016	0.997	0.805	0.794	1.158	0.988	1.023
$R_1(I > 2\sigma(I))$	0.0415	0.0397	0.0366	0.0492	0.0350	0.0411	0.0308
$wR_2(I > 2\sigma(I))$	0.0809	0.0731	0.0540	0.0982	0.0997	0.1027	0.0785
R_1(all data)	0.0777	0.0677	0.0783	0.0987	0.0488	0.0765	0.0418
wR_2(all data)	0.0921	0.0725	0.0614	0.1126	0.1061	0.1204	0.0845

Table S 3 Selected bond lengths (Å), angles (deg.) and distortion parameters in ***1****$_x$ with x = 1, 0.9, 0.75, 0.5, 0.25, 0.1 and 0.*

Parameters	**1$_1$**	**1$_{0.9}$**	**1$_{0.75}$**	**1$_{0.5}$**	**1$_{0.25}$**	**1$_{0.1}$**	**1$_0$**
	high-concentration materials (HCM)				**low-concentration materials (LCM)**		
Ref.	[2]	This work					
M-O1 (Å)	2.065(2)	2.0540(13)	2.052(2)	2.046(3)	1.9764(13)	1.965(2)	1.9660(12)
M-O2 (Å)	2.305(2)	2.3239(13)	2.353(2)	2.380(3)	2.701(2)	2.734(2)	2.7635(14)
M-O3 (Å)	2.084(2)	2.0761(12)	2.076(2)	2.070(3)	1.9995(12)	1.986(2)	1.9871(11)
M-O4 (Å)	2.207(2)	2.2154(13)	2.228(2)	2.237(3)	2.4826(14)	2.545(2)	2.5266(13)
M-N1 (Å)	2.085(2)	2.081(2)	2.084(2)	2.085(3)	2.063(2)	2.066(2)	2.0622(14)
M-N3 (Å)	2.105(2)	2.101(2)	2.091(2)	2.096(3)	2.044(2)	2.047(2)	2.0389(14)
C-O (Å)	1.254(3)-1.279(3)	1.252(2)-1.281(2)	1.251(3)-1.280(2)	1.244(5)-1.283(5)	1.240(2)-1.277(2)	1.233(3)-1.275(3)	1.232(2)-1.283(2)
O1-M-O3 (deg.)	145.49(8)	145.12(5)	144.91(7)	144.68(12)	129.80(6)	129.59(7)	127.93(5)
O1-M-O4 (deg.)	95.69(8)	95.67(5)	95.76(7)	95.77(11)	88.19(5)	89.34(7)	87.47(5)
O2-M-O3 (deg.)	93.42(7)	93.95(5)	93.73(6)	93.73(11)	84.57(5)	85.52(6)	83.67(5)
O2-M-O4 (deg.)	94.00(7)	93.10(5)	92.60(6)	91.84(10)	82.79(5)	83.40(7)	81.71(5)
N1-M-N3 (deg.)	95.01(9)	95.10(6)	95.46(8)	95.83(13)	105.28(6)	104.68(8)	105.96(6)

O-C-O (deg.)	119.3(3), 120.0(3)	118.8(2), 119.8(2)	119.4(2), 120.3(2)	119.8(4), 120.3(4)	120.0(2), 121.8(2)	120.0(2), 121.6(2)	120.5(2), 122.4(2)
O…N* (Å)	2.927(4), 2.941(4)	2.929(2), 2.938(2)	2.935(3), 2.937(3)	2.938(5), 2.939(5)	2.863(2), 2.947(2)	2.876(3), 2.955(3)	2.864(2), 2.953(2)
O…H* (Å)	2.10, 2.14	2.13, 2.15	2.13, 2.16	2.14, 2.16	2.03, 2.17	2.20, 2.06	2.04, 2.17
O-H-N* (deg.)	157, 159	161, 166	161, 167	168, 170	147, 156	147, 158	147, 156
O…N† (Å)	2.926(3), 2.964(3)	2.937(2), 2.971(2)	2.936(3), 2.965(3)	2.945(5), 2.956(5)	2.859(2), 2.927(2)	2.871(3), 2.934(3)	2.848(2), 2.917(2)
O…H† (Å)	2.06, 2.13	2.14, 2.15	2.14, 2.17	2.15, 2.19	2.00, 2.07	2.10, 2.03	1.99, 2.06
O-H-N† (deg.)	162, 169	164, 173	160, 175	158, 171	163, 166	163, 166	163, 166
Geometry of polyhedron ($S_Q(P)$)‡	MN_2O_4, Octahedron (4.116)	MN_2O_4, Octahedron (4.200)	MN_2O_4, Octahedron (4.217)	MN_2O_4, Octahedron (4.282)	MN_2O_2, Tetrahedron (1.191)	MN_2O_2, Tetrahedron (1.068)	MN_2O_2, Tetrahedron (1.035)

* Intramolecular H-bond

† Intermolecular H-bond (symmetry operations for $\mathbf{1_x}$ (x = 0.9, 0.75, 0.5) are -x+1, -y+2, -z+3 and x, -y+3/2, z-1/2; symmetry operations for $\mathbf{1_x}$ (x = 0.25, 0.1, 0) are x, -y+1/2, z-1/2; x, -y+1/2, z+1/2)

‡ Distortion of the MXn coordination polyhedron was characterized by *SQ(P)* value, which measures the deviation of its shape from the ideal symmetry. The analysis performed with SHAPE 2.1 software.[6,7]

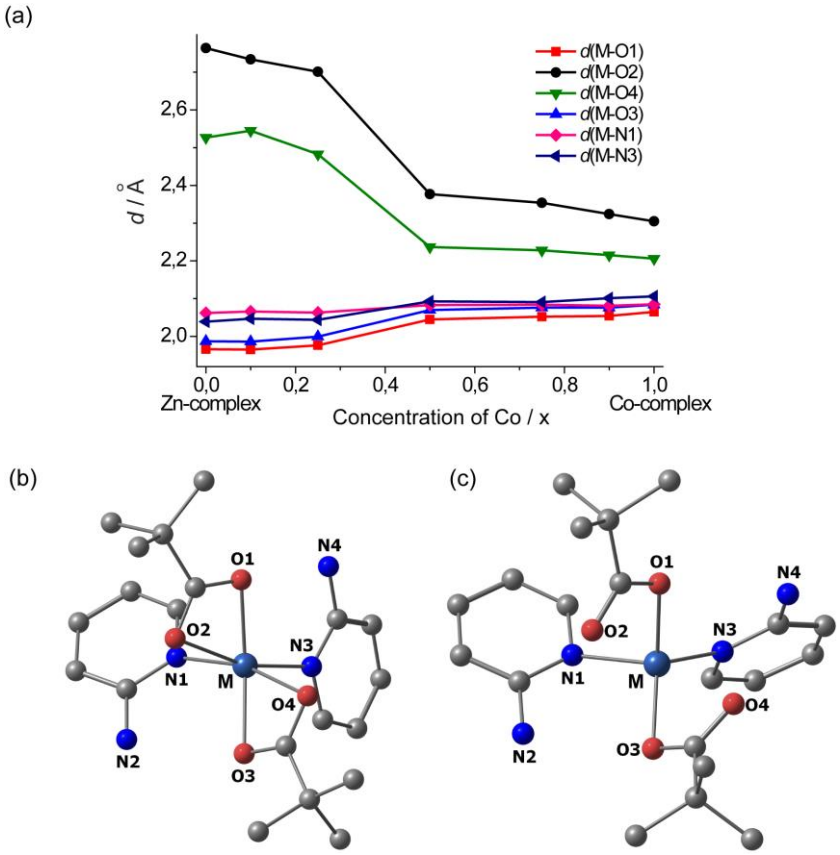

Figure S 1.(a) Concentration dependence of the metal-ligand bond lengths for $\mathbf{1}_x$ *with x = 1, 0.9, 0.75, 0.5, 0.25, 0.1 and 0, and corresponding structures of* $\mathbf{1}_1$ *(b) and* $\mathbf{1}_0$ *(c) in ball-and-stick representation. Metal ion: teal, O: red, N: blue, C: gray, H and counterion omitted.*

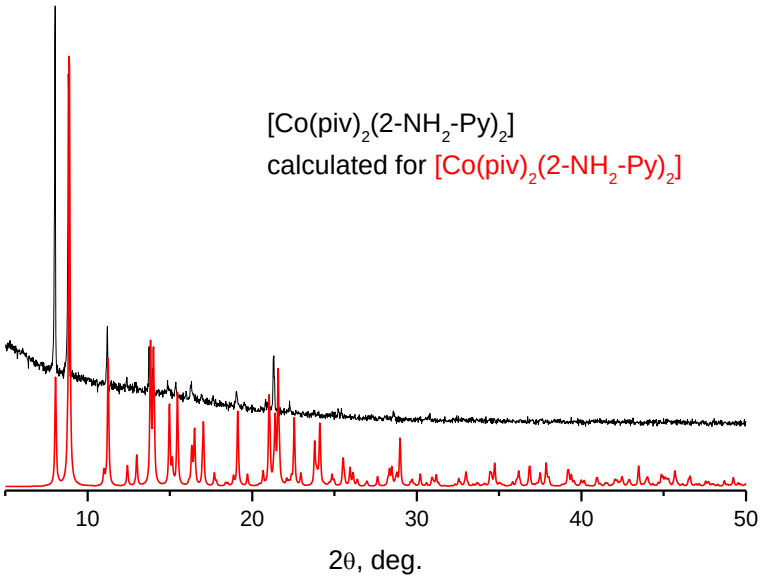

Figure S 2. Powder XRD pattern for compound $\mathbf{1_1}$*:* $[Co(piv)_2(2\text{-}NH_2\text{-}Py)_2]$ *(*λ *= 1.541 Å).*

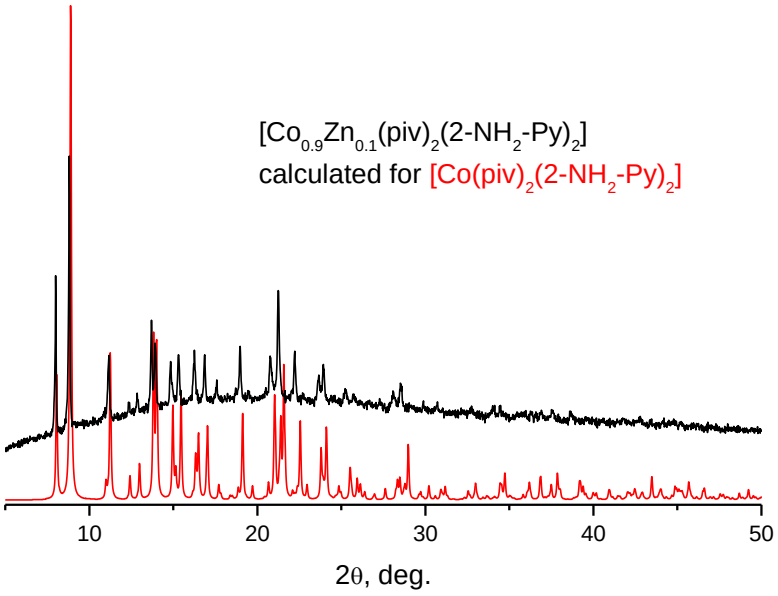

Figure S 3: Powder XRD pattern for compound ***1*** *$_{0.9}$: [Co$_{0.9}$Zn$_{0.1}$(piv)$_2$(2-NH$_2$-Py)$_2$] (λ = 1.541 Å).*

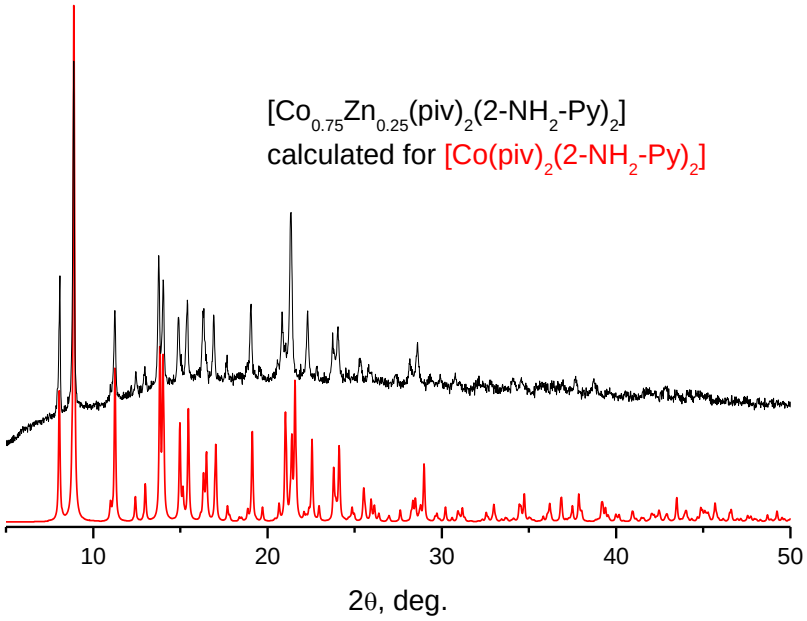

Figure S 4. Powder XRD pattern for compound ***1*** *$_{0.75}$: [Co$_{0.75}$Zn$_{0.25}$(piv)$_2$(2-NH$_2$-Py)$_2$] (λ = 1.541 Å).*

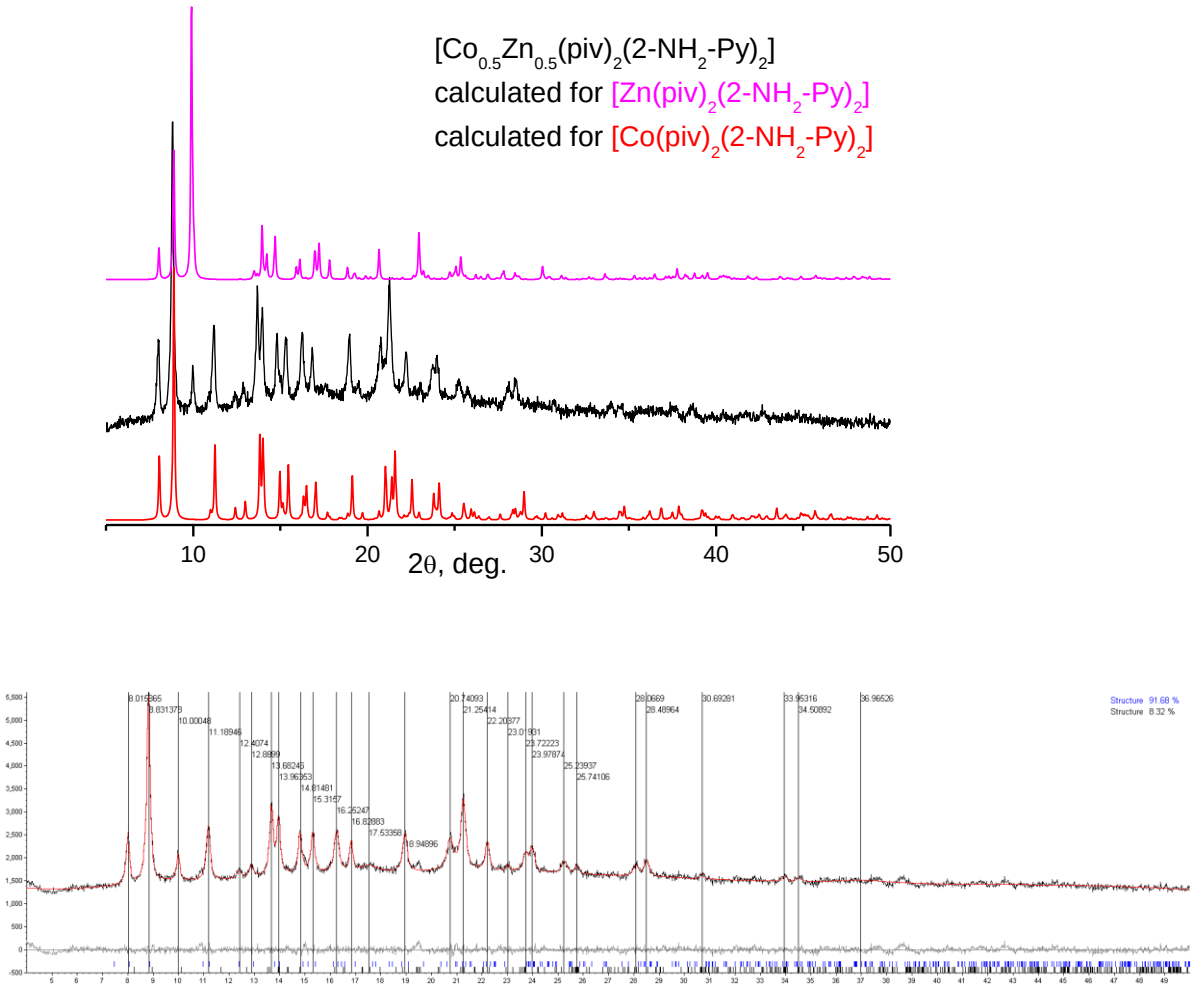

Figure S 5. Powder XRD pattern for compound ***1*****$_{0.5}$***: [$Co_{0.5}Zn_{0.5}(piv)_2(2\text{-}NH_2\text{-}Py)_2$] ($\lambda$ = 1.541 Å) and results of data analysis taking into account two phases.*

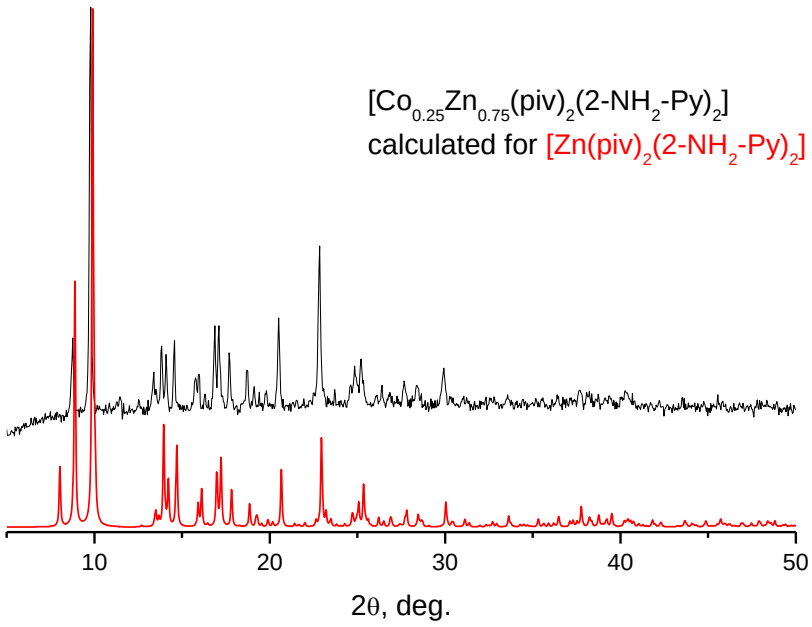

Figure S 6. Powder XRD pattern for compound ***1*****$_{0.25}$***: [$Co_{0.25}Zn_{0.75}(piv)_2(2\text{-}NH_2\text{-}Py)_2$] ($\lambda$ = 1.541 Å).*

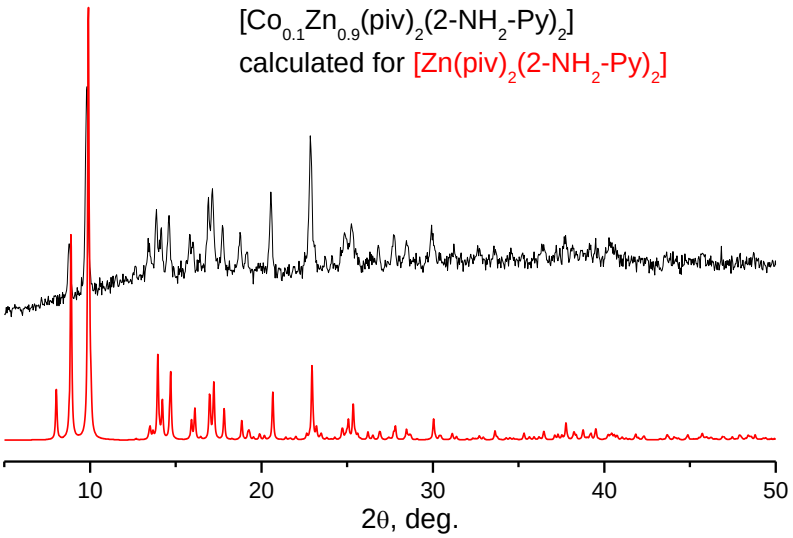

Figure S 7. Powder XRD pattern for compound ***1*****$_{0.1}$***: [$Co_{0.1}Zn_{0.9}(piv)_2(2\text{-}NH_2\text{-}Py)_2$] ($\lambda$ = 1.541 Å).*

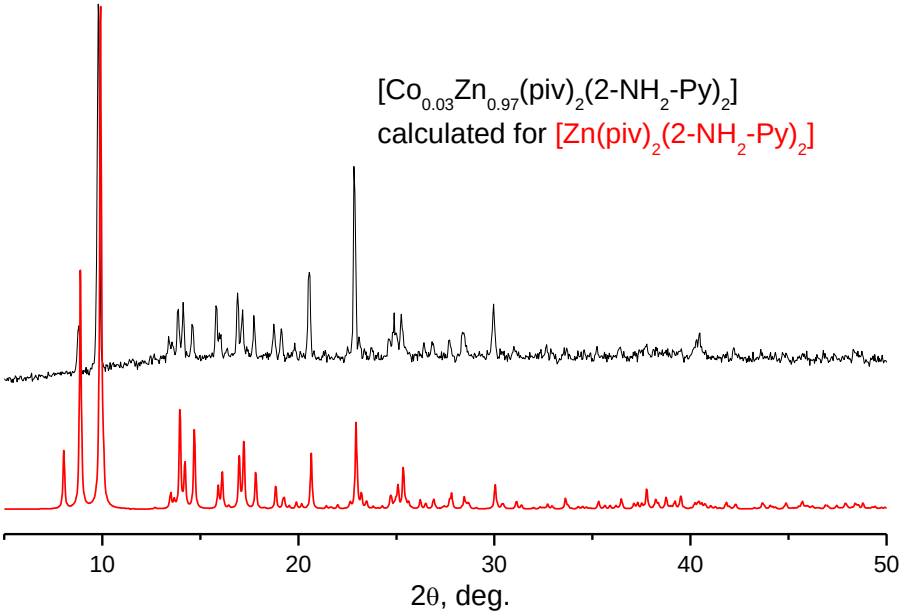

Figure S 8. Powder XRD pattern for compound ***1*** $_{0.03}$*: [Co*$_{0.03}$*Zn*$_{0.97}$*(piv)*$_2$*(2-NH*$_2$*-Py)*$_2$*] (λ = 1.541 Å).*

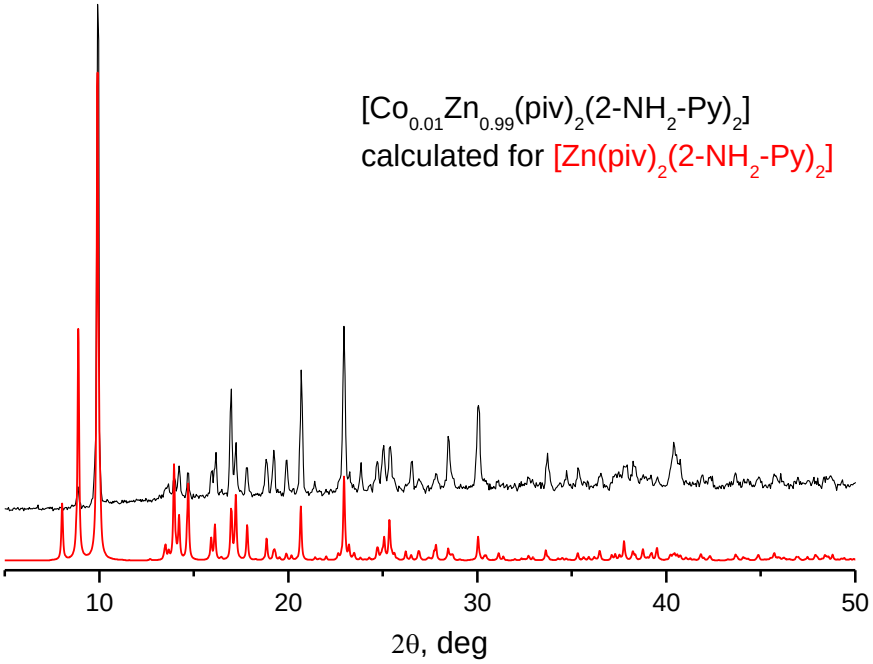

Figure S 9 Powder XRD pattern for compound ***1*** $_{0.01}$*: [Co*$_{0.01}$*Zn*$_{0.99}$*(piv)*$_2$*(2-NH*$_2$*-Py)*$_2$*] (λ = 1.541 Å).*

1.2. Mid-IR spectra and spectral bands assignment

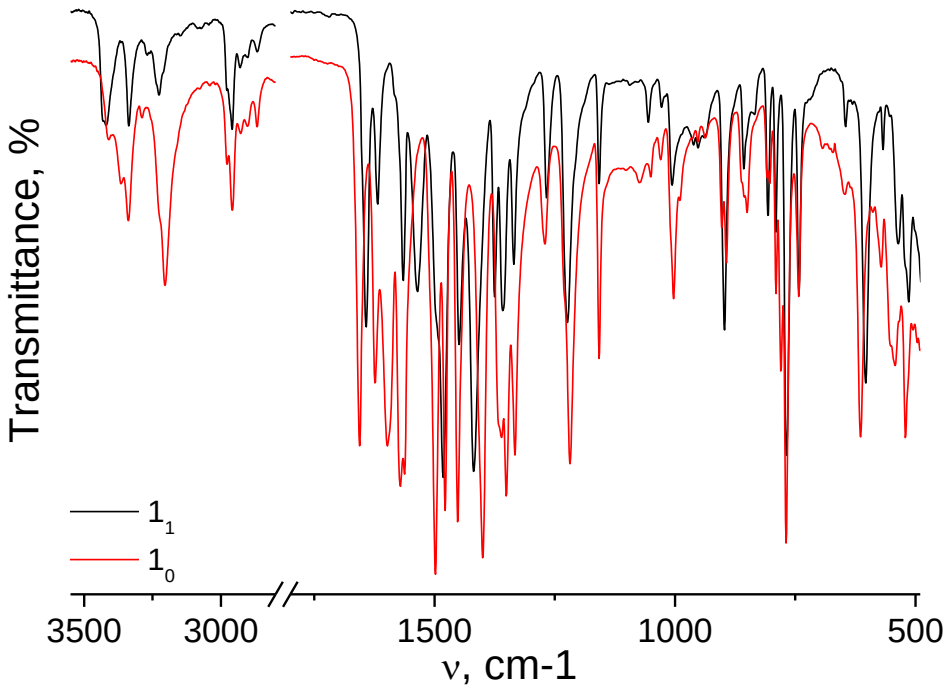

Figure S 10. IR spectra of ***1₁*** *and* ***1₀****.*

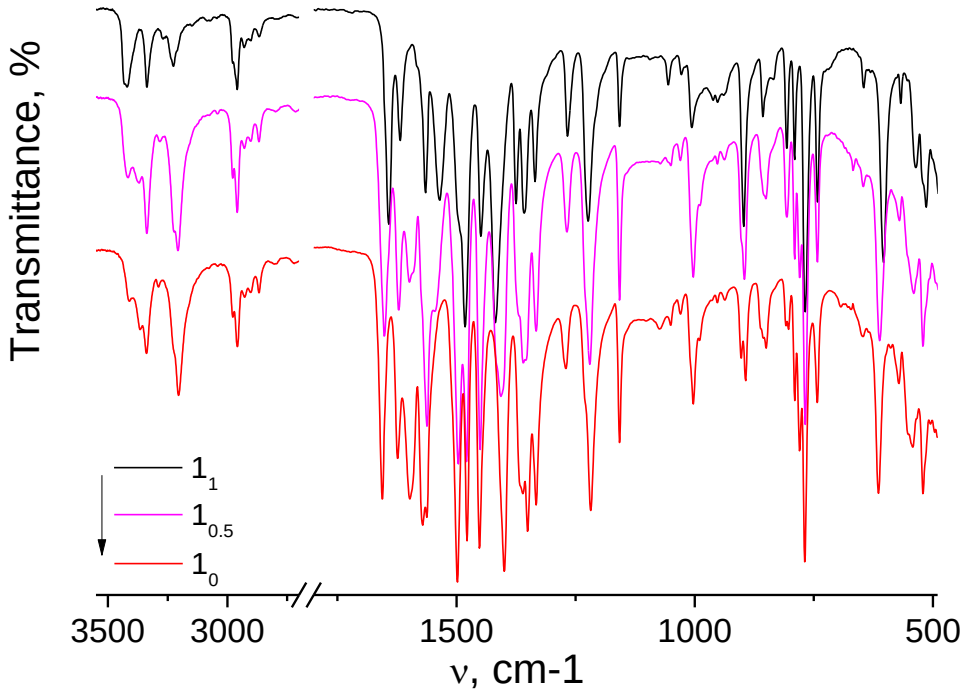

Figure S 11. IR spectra of ***1₁****,* ***1₀.₅****, and* ***1₀****.*

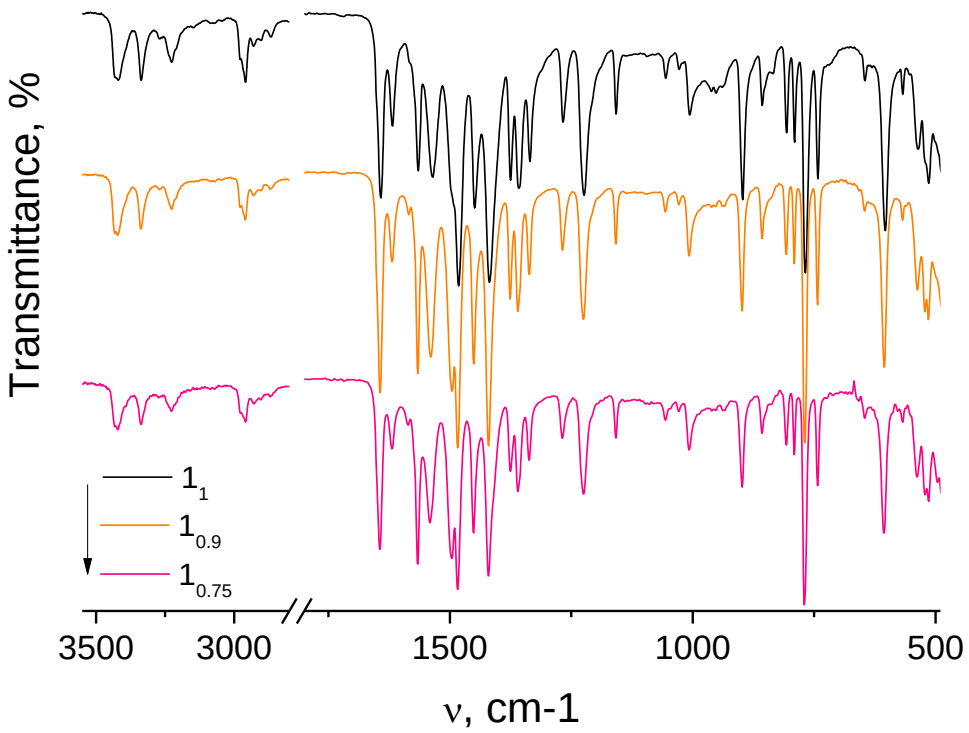

Figure S 12. IR spectra of $\mathbf{1}_{1}$, $\mathbf{1}_{0.9}$, *and* $\mathbf{1}_{0.75}$.

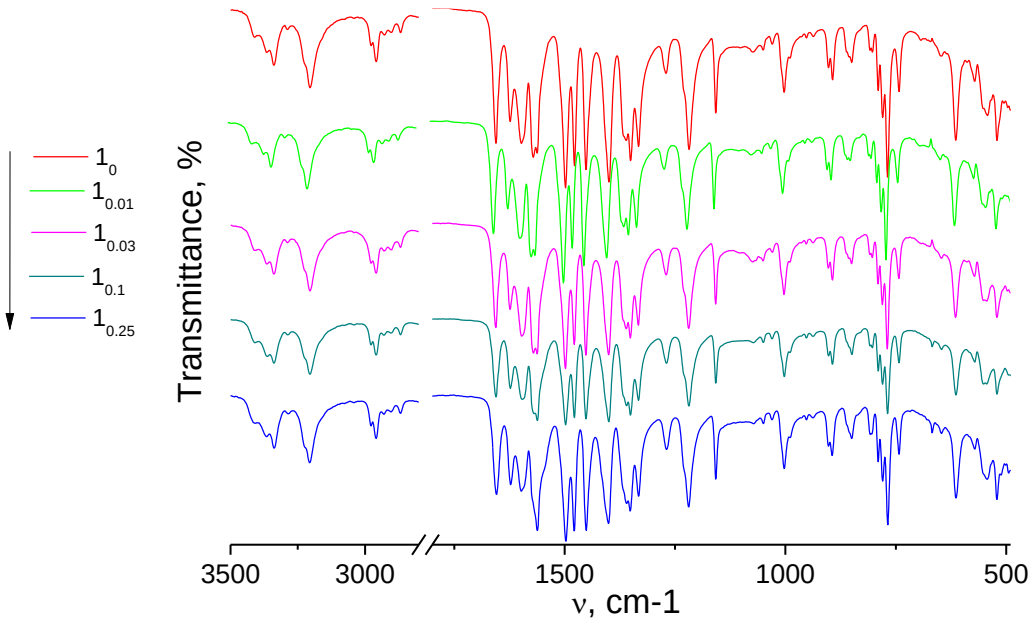

Figure S 13. IR spectra of $\mathbf{1}_{0}$, $\mathbf{1}_{0.01}$, $\mathbf{1}_{0.03}$, $\mathbf{1}_{0.1}$, *and* $\mathbf{1}_{0.25}$.

*Table S 4 The assignment of IR spectral bands for **1**$_1$ and **1**$_0$*

	1$_1$	**1**$_0$
ν_{as}(N-H(NH_2))	3420	3411
ν_{sym}(N-H(NH_2))	3337	3339
ν (additional combined frequency)	3226	3204
ν_{as} (C-H)	2959	2958
ν_{sym} (C-H)	2930 2901 2867	2928 2903 2868
δ(N-H(NH_2))	1642	1656
ν (C=N and C=C)	1618	1624
ν_{as}(N-H(NH_2))	1565	1598
ν_{as}(COO^-)	1537	1571 1562
ν (C=N and C=C)	1482	1499 1478
δ_{as}(CH_3)	1449	1452
ν_{sym}(COO^-)	1419	1400
δ_{sym}(CH_3)	1376 1358 1335	1360 1351 1333
δ(C-H, aromatic ring)	1267	1269
γ($C(CH_3)_3$)	1224	1219
δ(C-H, aromatic ring)	1006 897	1003 902 893
δ(COO^-)	806 790 768 742	790 780 769 743

2. THz-EPR

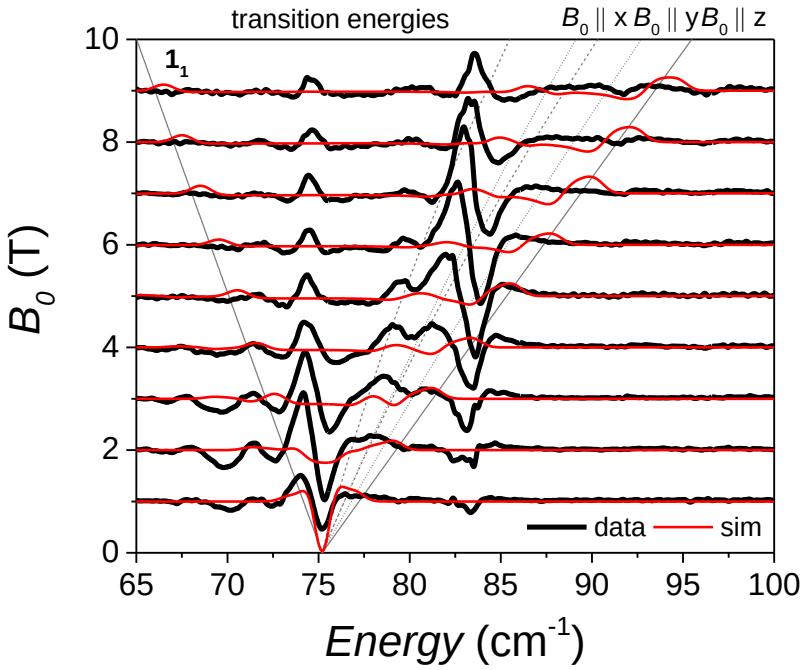

Figure S 14. THz-EPR spectra of ***1****$_1$. Shown are MDS spectra obtained by dividing a spectrum measured at B_0 -1 T by a spectrum measured at B_0. Data (black lines) is rescaled for better visibility and offset according to B_0. Simulations with Eq. 1 and D = 36.7 cm^{-1},E = 4.5 cm^{-1}, $g_\perp$ = 2.53, $g_{||}$ = 2.21 are shown as red lines. Calculated transition energies for magnetic field applied along the principal axes x, y, and z of Eq. 1 are shown as gray dashed, dotted, and solid lines.*

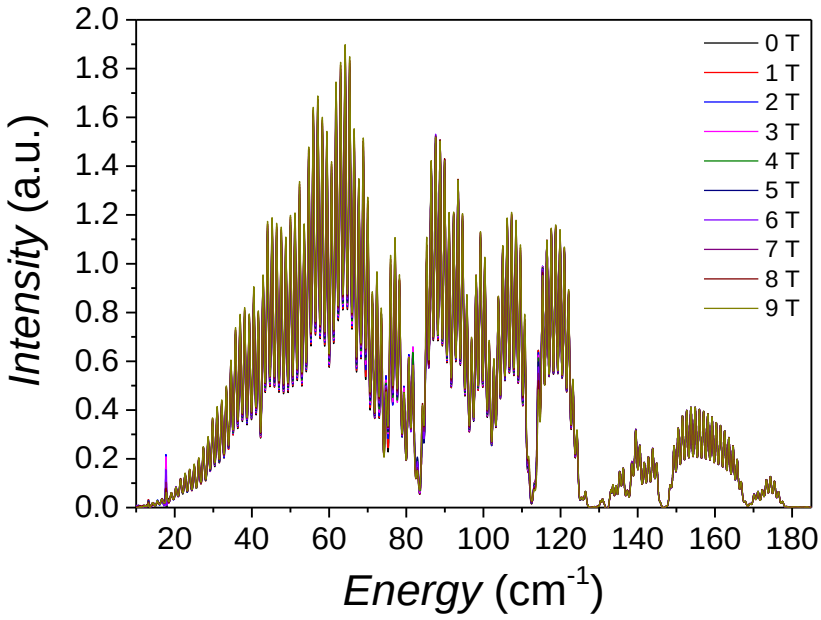

Figure S 15. Raw spectra used to obtain the spectra shown in Figure S 14.

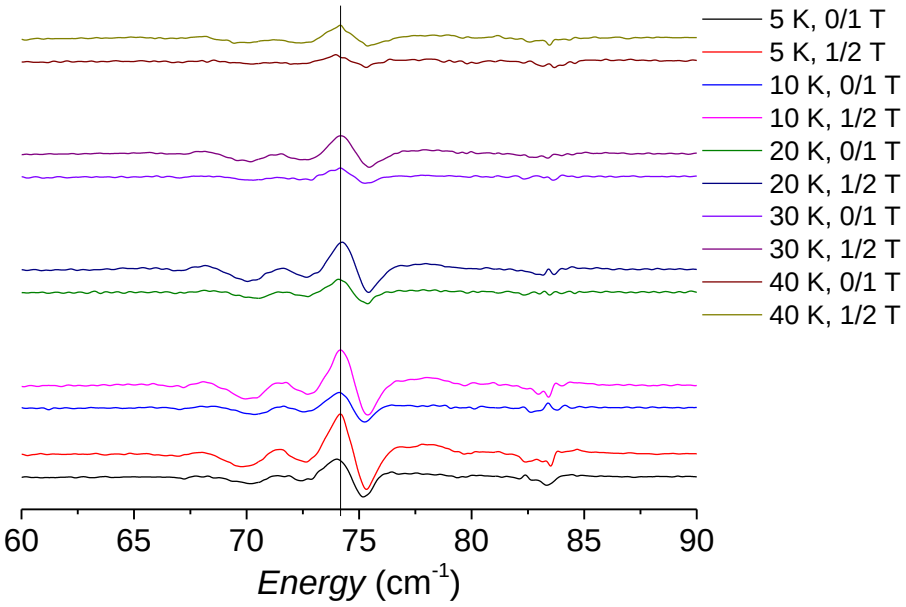

Figure S 16. Temperature dependent THz-EPR spectra of ***1*** *$_1$. Shown are MDS spectra recorded at the indicated temperatures. Data is offset for clarity. The vertical line is a guide for the eye following the maximum in the MDS spectra.*

In the following plot the MDS spectra are shown with the raw spectra as measured. Apart from the magnetic feature at 75 and 49 cm^{-1}, variations in the MDS are due to vanishing transmitted radiation intensity. The variations in the MDS at 36 cm^{-1} is due to 50 Hz noise and its position in the spectrum can be changed by adjusting the scanner velocity, which was 20 kHz for the here shown spectra.

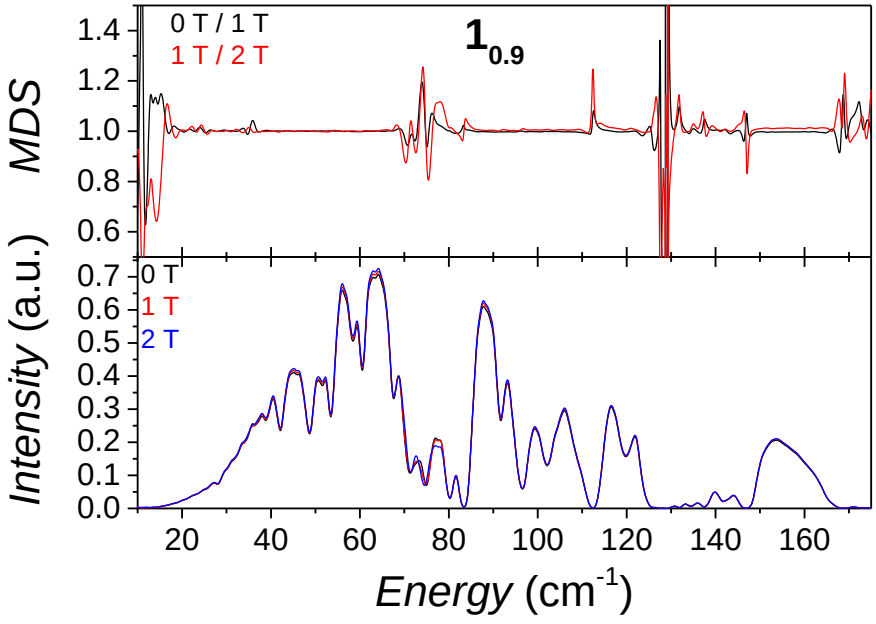

Figure S 17. THz-EPR spectra of ***1*** *$_{0.9}$. In the upper plot the MDS are shown and in the bottom plot the raw spectra used for the construction of the MDS are shown.*

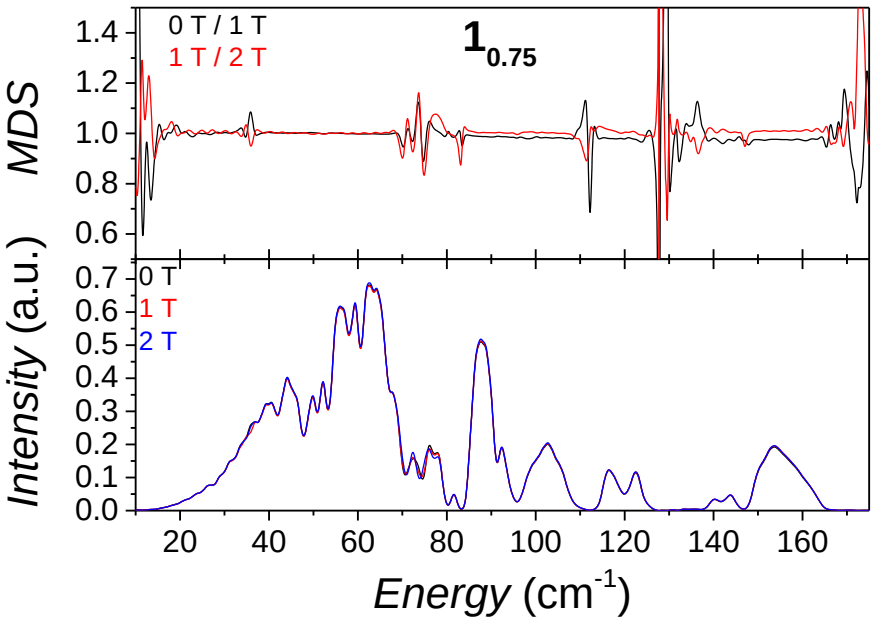

Figure S 18. THz-EPR spectra of $\mathbf{1}_{0.75}$*. In the upper plot the MDS are shown and in the bottom plot the raw spectra used for the construction of the MDS are shown.*

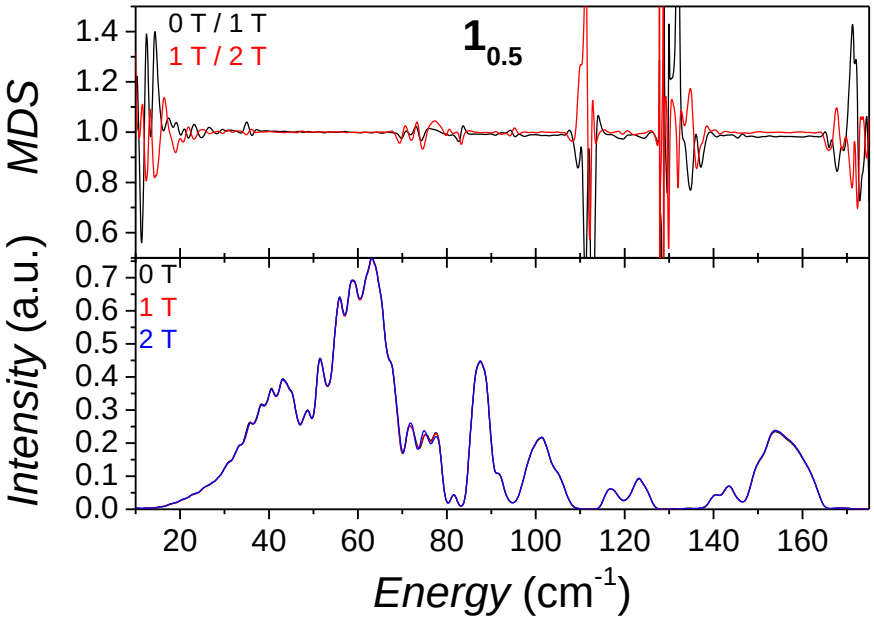

Figure S 19. THz-EPR spectra of $\mathbf{1}_{0.5}$*. In the upper plot the MDS are shown and in the bottom plot the raw spectra used for the construction of the MDS are shown.*

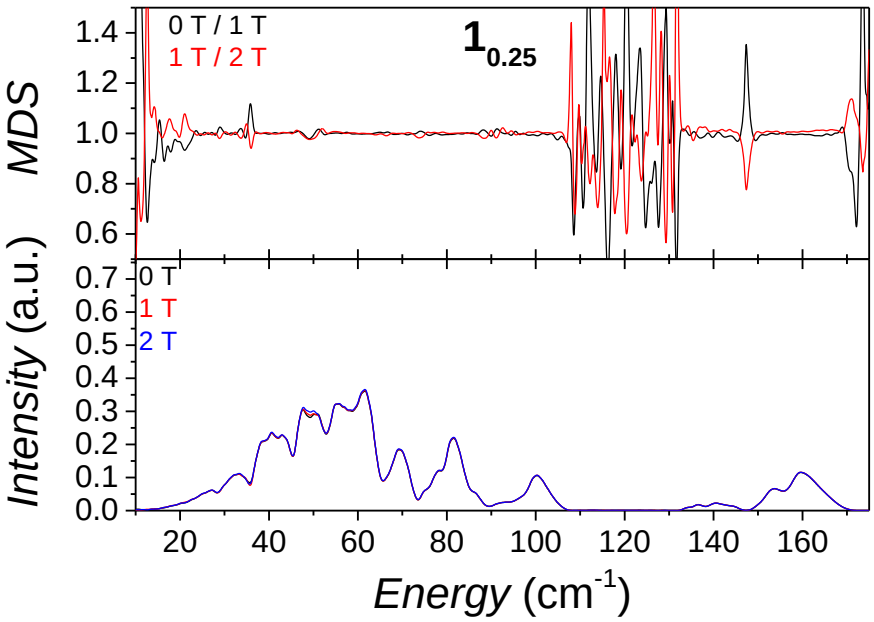

Figure S 20. THz-EPR spectra of $\mathbf{1}_{0.25}$*. In the upper plot the MDS are shown and in the bottom plot the raw spectra used for the construction of the MDS are shown.*

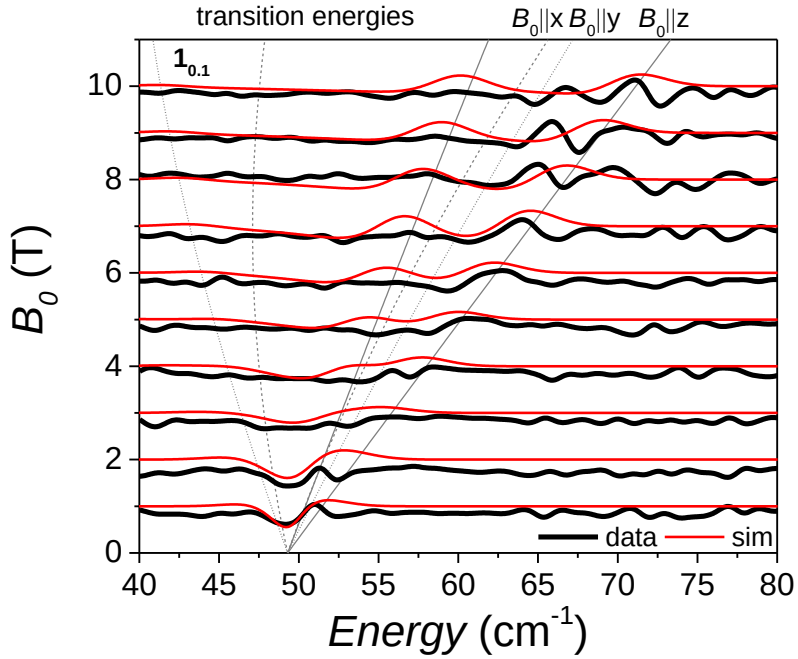

Figure S 21. THz-EPR spectra of $\mathbf{1}_{0.1}$*. Shown are MDS spectra obtained by dividing a spectrum measured at* B_0 *-1 T by a spectrum measured at* B_0*. Data (black lines) is rescaled for better visibility and offset according to* B_0*. Simulations with Eq. 1 and* $D = -23.9\ cm^{-1}$*,* $E = 3.1\ cm^{-1}$*,* $g_\perp = 2.25$*,* $g_{||} = 2.38$ *are shown as red lines. Calculated transition energies for magnetic field applied along the principal axes x, y, and z of Eq. 1 are shown as gray dashed, dotted, and solid lines.*

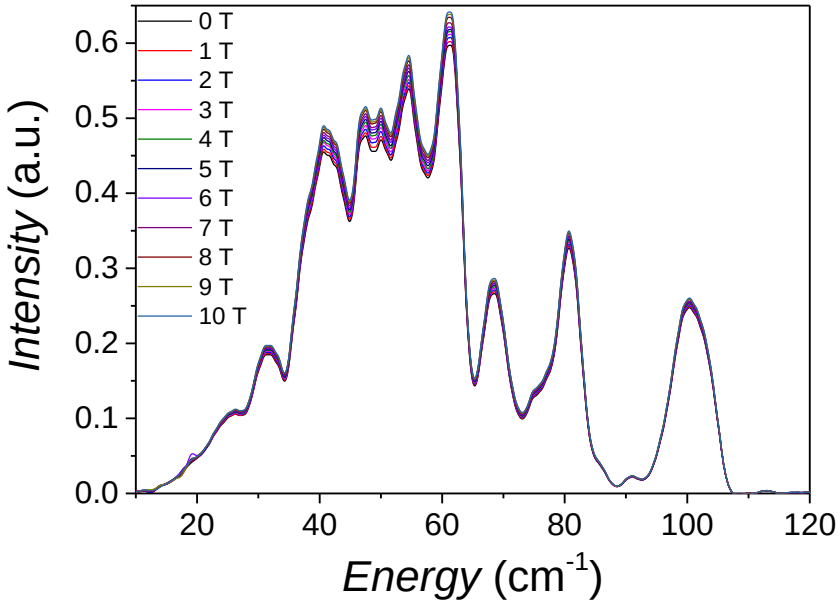

Figure S 22. Raw spectra used to construct the MDS spectra shown in Figure S 21.

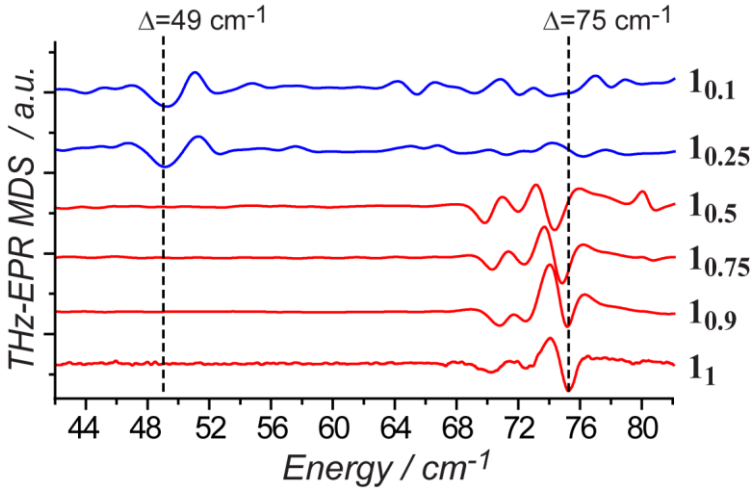

*Figure S 23. THz-EPR magnetic field division spectra for LCM (**1**$_{0.25}$ and **1**$_{0.1}$; blue lines) and HCM (**1**$_1$, **1**$_{0.9}$, **1**$_{0.75}$ and **1**$_{0.5}$; red lines). Dashed vertical lines are a guide for the eye and mark Δ = 75 cm^{-1} and Δ = 49 cm^{-1}. THz-EPR magnetic field division spectra (MDS) were achieved by dividing spectra measured at an external magnetic field $B = 0\,T$ by a reference spectrum measured at $B = 1\,T$.*

3. CW X-Band EPR

Continuous-wave X-Band EPR experiments were performed on **1**$_1$, **1**$_{0.9}$, **1**$_{0.75}$, **1**$_{0.5}$, **1**$_{0.25}$, **1**$_{0.1}$, **1**$_{0.03}$, and **1**$_{0.01}$. Experiments were performed at a temperature of 10 K and a microwave frequency of 9.69 GHz.

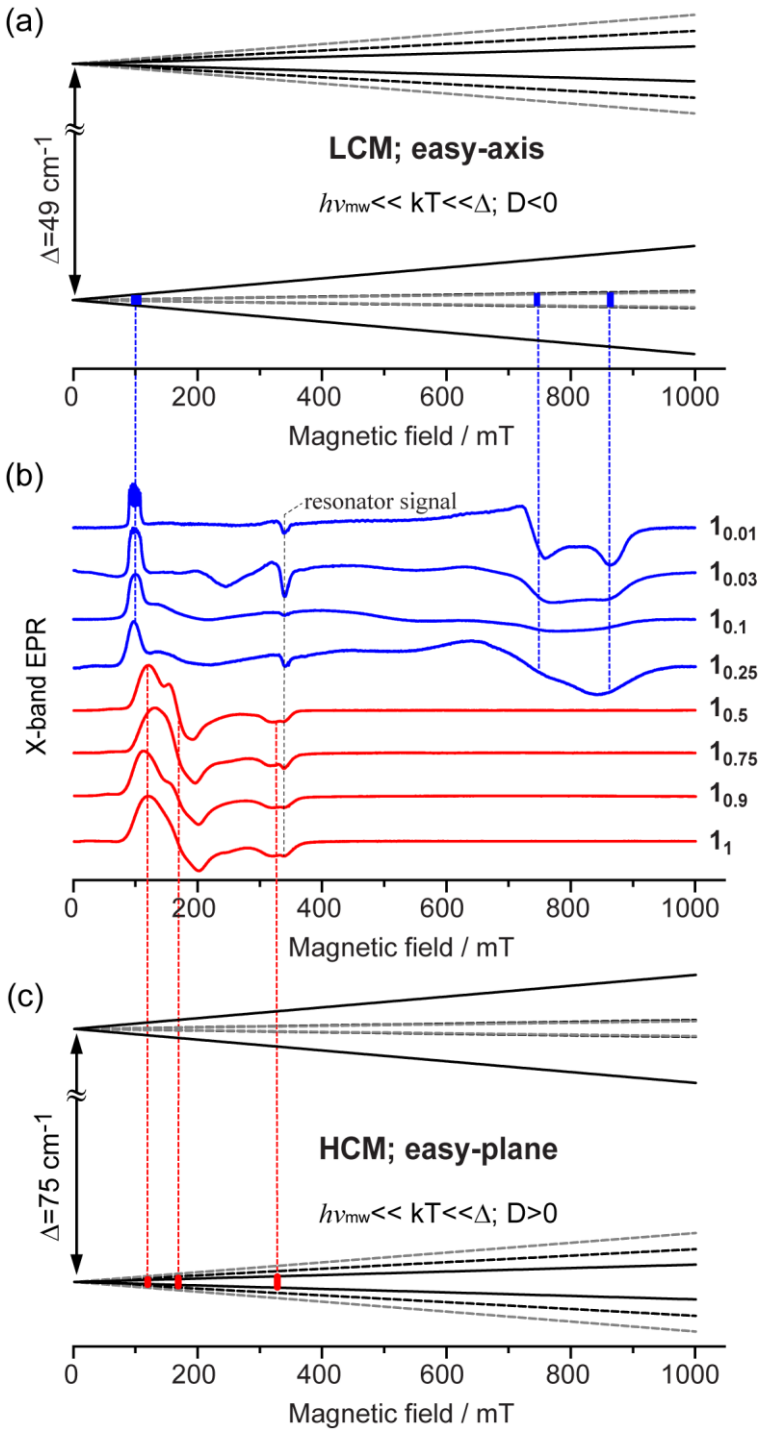

Figure S 24 Overview of X-Band EPR experimental results. In the middle panel (b) the experimental spectra are shown, with those of LCM and HCM in blue and red, respectively. In panels (a) and (c) schematic energy diagrams for LCM (a) and HCM (c) are shown. The splitting with magnetic field is depicted for magnetic field applied parallel to the main anisotropy axis (solid black lines) and perpendicular to it (black and gray dashed lines). X-Band EPR transitions within the ground-state duplet are indicated by blue/red bars.

An overview over the experimental results is shown in Figure S 24. The spectra of HCM were observed as quite similar with three observed EPR lines at roughly 115, 170, and 325 mT. Spectra of LCM differed substantially from that. Although they differ significantly in shape and to which extent hyperfine lines could be resolved, they might be summarized as all revealing three EPR lines at fields of approximately 100, 745 and 875 mT. Taking into account that Δ is much larger than both the temperature and the microwave energy, the observed EPR lines can be assigned to transitions in the ground state duplet. First, the observation of three lines, for both HCM and LCM, indicate that each has a non-vanishing rhombicity, i.e. $E \neq 0$. Furthermore, from the resonance fields we can infer the ground state duplet and thereby the anisotropy. The corresponding energy diagrams with resonance fields are shown in Figure S 24. For a half-integer spin system with easy-plane anisotropy applying a field in that plane results in large energy splittings and subsequently low resonance fields. The minimum spin projection along the hard axis is non-vanishing. In fact, it is the same as for a single free electron and therefore the third, and highest, resonance field is closer to that expected for a free electron. On the contrary for a system with easy-axis anisotropy, applying a field along that direction lead to a low resonance field. Applying a field perpendicular to this axis lead to quite large resonance fields. Therefore, it is straightforward to assign HCM to easy-plane and LCM to easy-axis anisotropy. After this qualitative analysis, we analyze the data more thoroughly in four steps. First, the individual spectra are analyzed with an effective $S' = 1/2$ model. This model solemnly relies on the X-Band EPR results (although it is only meaningful and successful if Δ is much larger than both the temperature and the microwave energy). The thereby obtained effective g' parameters can be compared to, e.g., ab initio results (see Table S 10). Second, an $S = 3/2$ model will be used, with Δ fixed to the value obtained by THz-EPR. Third, we test whether a single set of parameters can be used for all LCM and HCM, respectively. Finally, we probe the effect of a rhombic g tensor on the spectrum of $\mathbf{1}_{0.01}$.

3.1. Effective S' = ½ model

$$\hat{H}_{1/2} = \mu_B \boldsymbol{B}_0 \cdot diag\left(g'_x, g'_y, g'_z\right) \cdot \hat{\boldsymbol{S}}' + \hat{I}_z A'_{zz} \hat{S}'_z \qquad (S1)$$

Table S 5: Best-fit parameters of X-band EPR spectra with the above given Hamiltonian in the effective S' = ½ model. lwpp and g-strain describe line-broadening mechanism, with the former a uniform Gaussian broadening resulting in a peak-to-peak distance of lwpp in the simulated derivative spectrum and the latter an isotropic Gaussian broadening in the three g factors. A_{zz} describes the hyperfine interaction with the I =7/2 ^{59}Co nuclei (the last term in the above Hamiltonian, further components of the hyperfine tensor could not be resolved and are neglected henceforth). rms is the square root of the mean of the squared deviations between simulation and experiment. It was not feasible to fit the spectrum of $\mathbf{1}_{0.1}$ with least-squares fitting techniques, therefore the fitting was performed manually.

Sample	g'_x	g'_y	g'_z	lwpp / mT	g-strain	A'_{zz} / MHz	rms
$\mathbf{1}_{0.01}$	0.93	0.79	7.03	1	0.036	235	0.0968
$\mathbf{1}_{0.03}$	0.95	0.80	6.95	2	0.07	235	0.1782
$\mathbf{1}_{0.1}$	0.93	0.82	6.85	4	0.09	235	0.1730
$\mathbf{1}_{0.25}$	0.87	0.87	7.15	20	0.17	-	0.1736
$\mathbf{1}_{0.5}$	5.89	4.09	2.11	28	-	-	0.0287
$\mathbf{1}_{0.75}$	5.57	4.08	2.10	37	-	-	0.0209
$\mathbf{1}_{0.9}$	5.94	4.30	2.10	40	-	-	0.0564
$\mathbf{1}_{1}$	5.88	4.11	2.11	44	-	-	0.0334

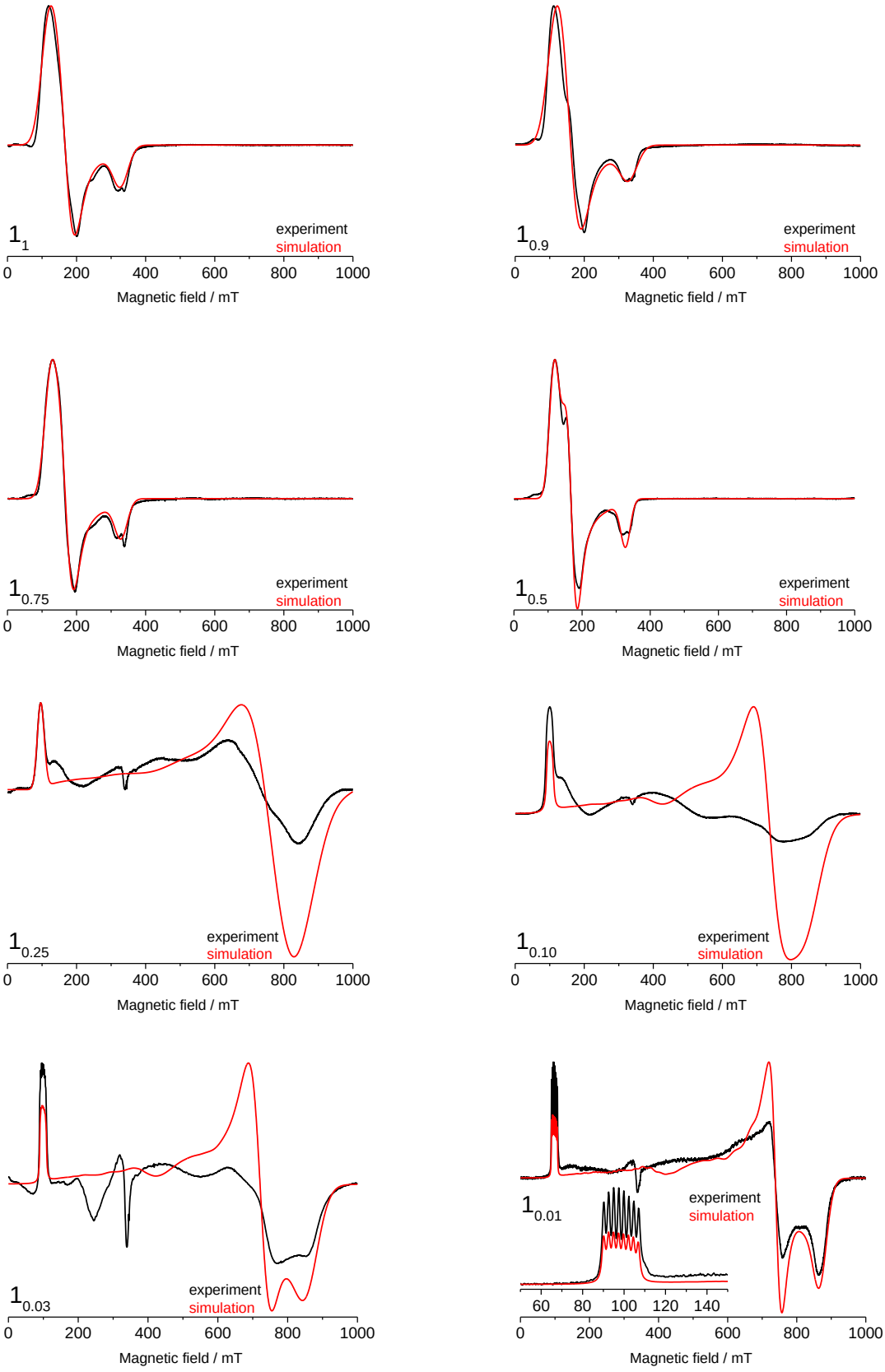

Figure S 25: Experimental X-Band EPR spectra (black lines) compared to simulations (red lines) with best-fit parameters in the effective S' = ½ model. The parameters are given in Table S 5.

3.2. $S = 3/2$ model

In the following fits with Eq. 1 of the main text are used. In this fits Δ was fixed to the values obtained from THz-EPR experiments. Hyperfine interactions with the I =7/2 ^{59}Co nuclei (when resolved) are described by the following Hamiltonian:

$$\widehat{H}_{\mathrm{HFI}} = \hat{I}_z A_{zz} \hat{S}_z \qquad (S2)$$

Table S 6: Best-fit parameters of X-band EPR spectra with eq 1. of the main text in S = 3/2 model. lwpp and E-strain describe line-broadening mechanism, with the former a uniform Gaussian broadening resulting in a peak-to-peak distance of lwpp in the simulated derivative spectrum and the latter an isotropic Gaussian broadening in the E parameter. A_{zz} describes the hyperfine interaction with the I =7/2 ^{59}Co nuclei. rms is the square root of the mean of the squared deviations between simulation and experiment. For the samples **$1_{0.25}$**, **$1_{0.1}$**, **$1_{0.03}$** *and* **$1_{0.01}$** *the values of $g_\perp$ were fixed at 2.25. The samples showing most resolved experimental spectra among HCM and LCM (***$1_{0.5}$** *and* **$1_{0.01}$***) and corresponding simulation parameters are highlighted.*

Sample	$g_\perp$	$g_{\|\|}$	D / cm^{-1}	$\|E\|$ / cm^{-1}	lwpp / mT	E-strain / cm^{-1}	A_{zz} / MHz	rms
$1_{0.01}$	2.25	2.38	-23.89	3.14	1	0.18	80	0.1238
$1_{0.03}$	2.25	2.36	-23.86	3.22	2	0.27	80	0.1837
$1_{0.1}$	2.25	2.35	-23.80	3.33	4	0.50	80	0.1645
$1_{0.25}$	2.25	2.44	-23.91	3.12	18	0.57	-	0.1675
$1_{0.5}$	2.53	2.21	36.66	4.53	29	-	-	0.0229
$1_{0.75}$	2.43	2.17	36.90	3.84	37	-	-	0.0202
$1_{0.9}$	2.65	2.23	36.43	5.16	42	-	-	0.0440
1_1	2.54	2.21	36.63	4.64	42	-	-	0.0317

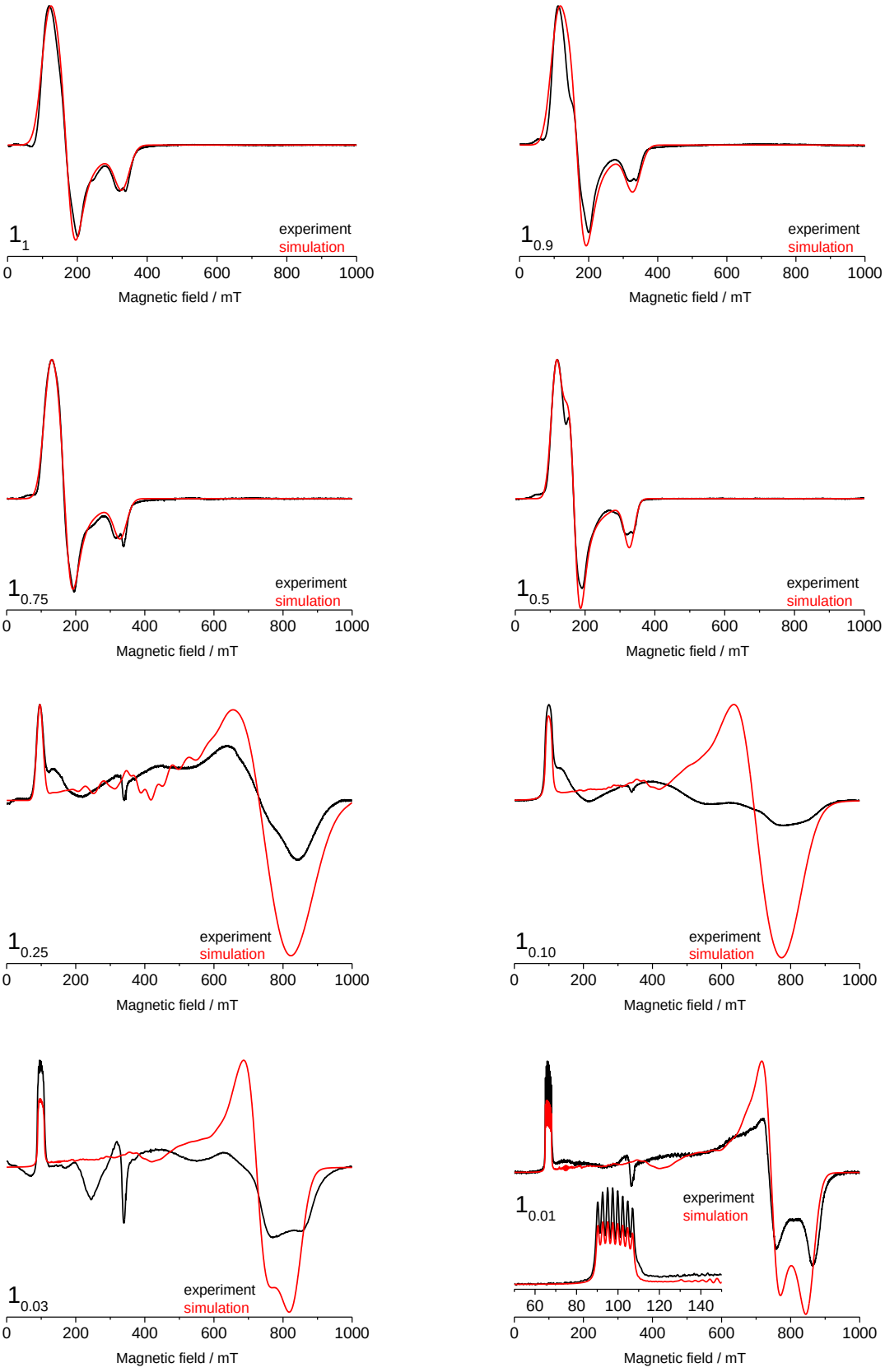

Figure S 26: Experimental X-Band EPR spectra (black lines) compared to simulations (red lines) with best-fit parameters in the S = 3/2 model. The parameters are given in Table S 6.

3.3. Generalized Parameters

As generalized parameters for HCM and LCM we chose those of $\mathbf{1}_{0.5}$ and $\mathbf{1}_{0.01}$.The only remaining adjustable parameters are those describing the linewidth. Overall comparison is shown in Figure S 27. Detailed comparison for each sample is shown in Figure S 28.

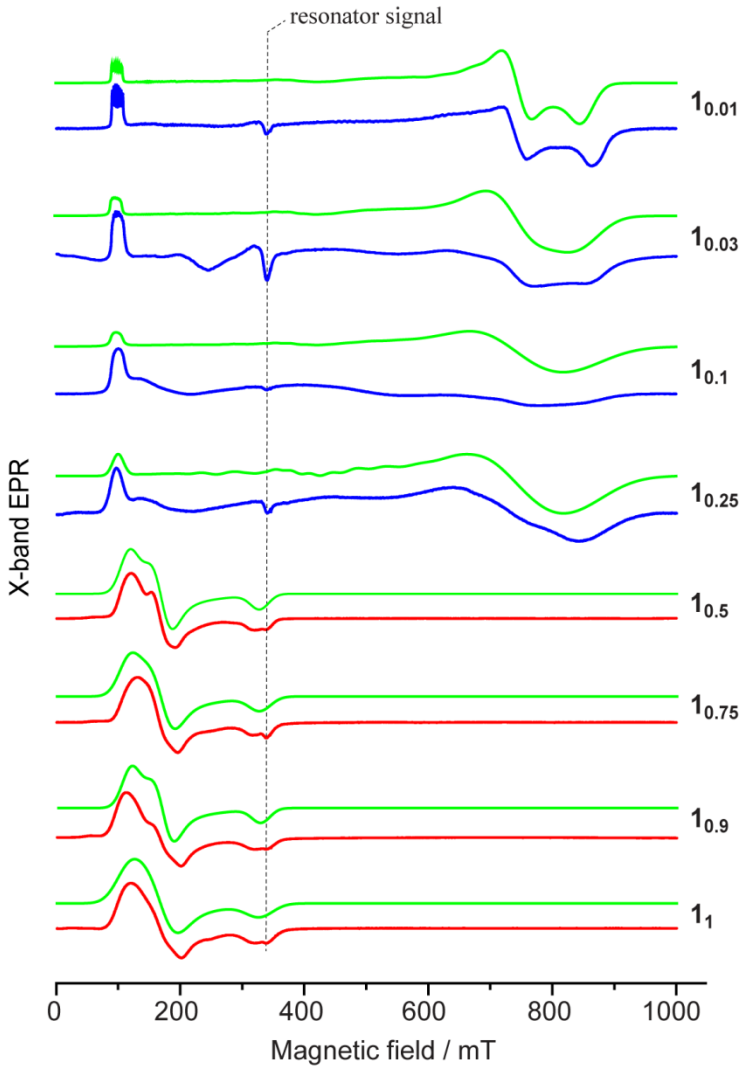

Figure S 27: X-band EPR spectra of LCM ($\mathbf{1}_{0.25}$, $\mathbf{1}_{0.1}$, $\mathbf{1}_{0.03}$ and $\mathbf{1}_{0.01}$; blue lines) and HCM ($\mathbf{1}_{1}$, $\mathbf{1}_{0.9}$, $\mathbf{1}_{0.75}$ and $\mathbf{1}_{0.5}$; red lines) and corresponding simulations (green lines). Experimental parameters of the spectra are mentioned in the main text. HCM spectra were simulated using the following EPR parameters: D = 36.66 cm^{-1}, E = 4.53 cm^{-1}, $g_{\perp}$ = 2.53, $g_{||}$ = 2.21. EPR parameters for simulation of LCM spectra were the following: D = -23.89 cm^{-1}, E = 3.14 cm^{-1}, $g_{\perp}$ = 2.25, $g_{||}$ = 2.38. Linewidth and E-strain were varied to fit the experimental spectra.

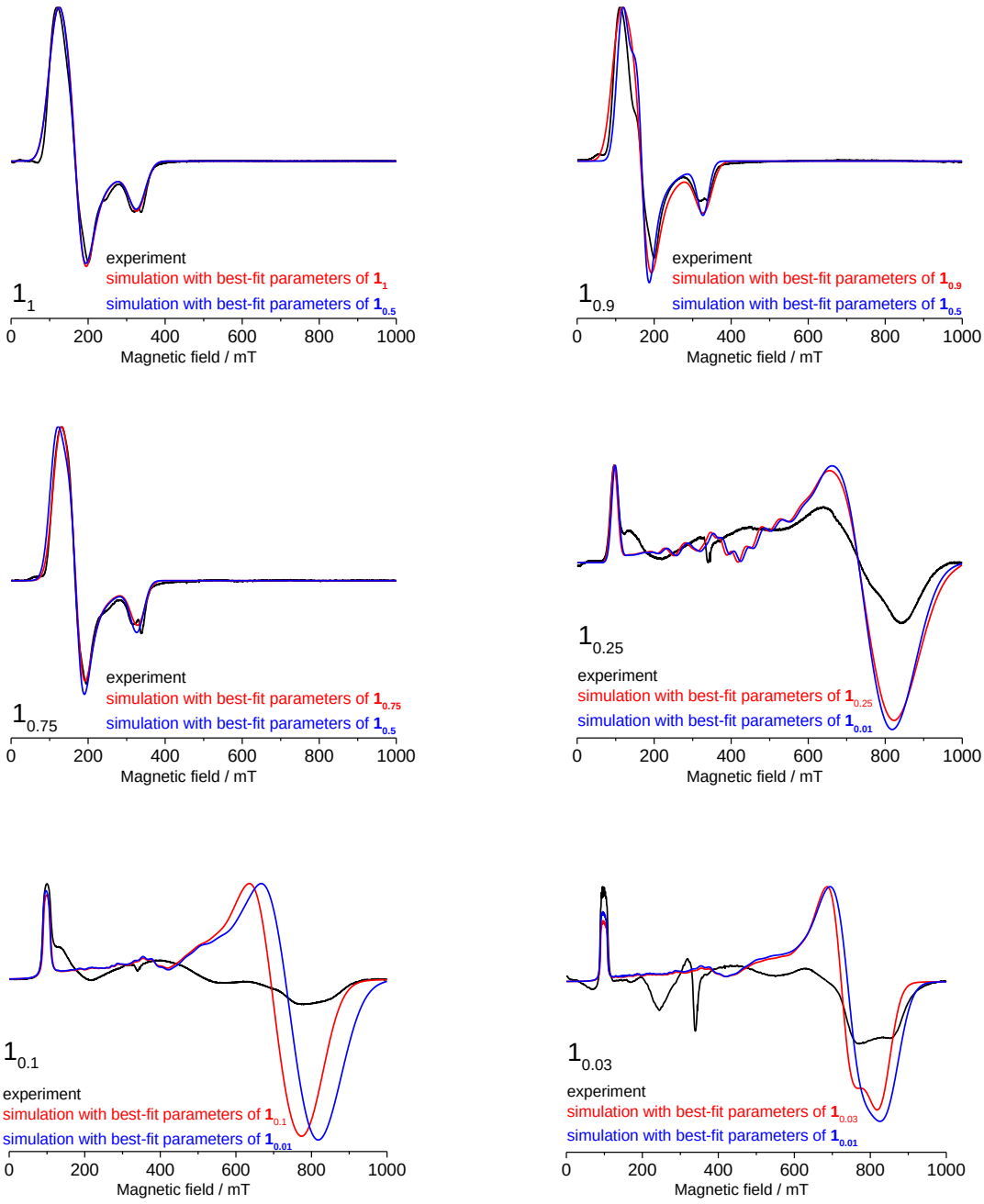

Figure S 28: Experimental X-Band EPR spectra (black lines) compared to simulations (red lines) with best-fit parameters in the S = 3/2 model. The parameters are given in Table S 6. In blue are simulations with the generalized parameter sets shown.

3.4. Simulation of experimental EPR spectrum of $\mathbf{1_{0.01}}$ with S=3/2 model assuming axial and rhombic *g*-tensor

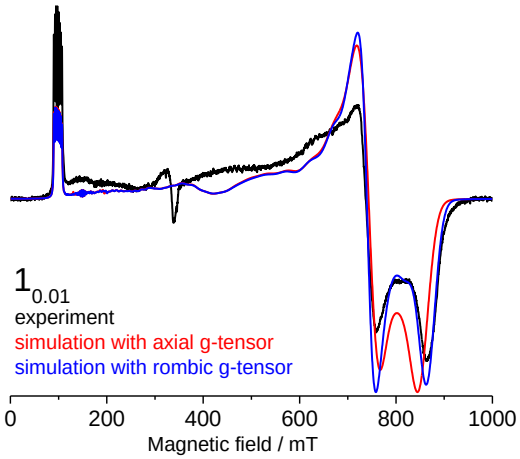

Figure S 29: Experimental and simulated spectra of $\mathbf{1_{0.01}}$. *Simulations with axial g tensor (red line) use the following parameters: S = 3/2,* $\boldsymbol{g}$ *= diag(2.25, 2.25, 2.38), D = - 23.89 cm*$^{-1}$*, |E| = 3.14 cm*$^{-1}$*, E-strain = 0.18 cm*$^{-1}$*,* A_{zz} *= 80 MHz and an additional Lorentzian line broadening with 1 mT FWHM. Simulations with rhombic g tensor (blue line) use the following parameters: S = 3/2,* $\boldsymbol{g}$ *= (2.15, 2.20, 2.38), D = - 23.85 cm*$^{-1}$*, |E| = 3.23 cm*$^{-1}$*, E-strain = 0.13 cm*$^{-1}$*,* A_{zz} *= 80 MHz and an additional Lorentzian line broadening with 1 mT FWHM.*

4. AC Susceptibility

AC magnetic susceptibility data was collected on a Quantum Design MPMS-XL SQUID magnetometer on finely ground polycrystalline powders (~20 mg) in the temperature range of 2 - 5 K under a DC field of 0.2 T and an AC field of 0.35 mT oscillating in a frequency range of 0.1 - 1500 Hz.

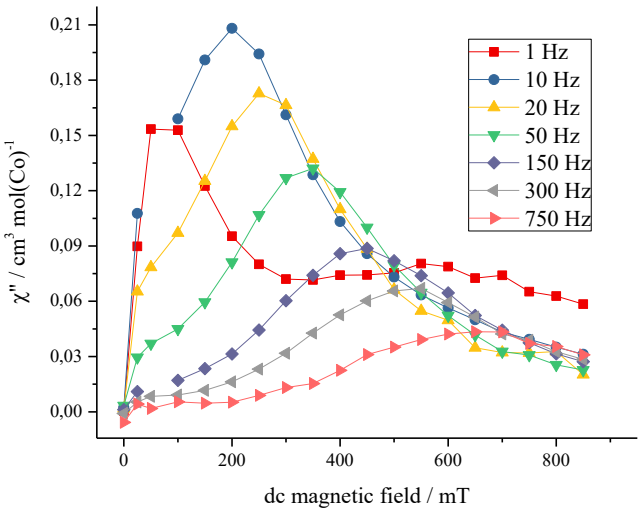

Figure S 30. Out of phase component χ'' of the AC magnetic susceptibility of ***1*** $_{0.75}$ *as function of the DC magnetic field for various AC frequencies measured at a temperature of 2 K.*

First experiments on **1**$_{0.75}$ revealed that, in the absence of a DC magnetic field, unfortunately no significant out-of-phase susceptibility χ" could be detected even at the highest frequencies and lowest temperature. However, under an applied DC field clear out-of-phase susceptibility χ" was detected (see Figure S 30). For the further experiments we chose the DC magnetic field with maximum χ" at 10 Hz, i.e. 200 mT. In Figure S 31 the in-phase χ' (left) and out-of-phase χ" (right) components of the AC magnetic susceptibilities measured at different temperatures and an applied DC field of 200 mT are shown as function of AC frequency ν. In the whole section the data is normalized to one mol of Co molecules.

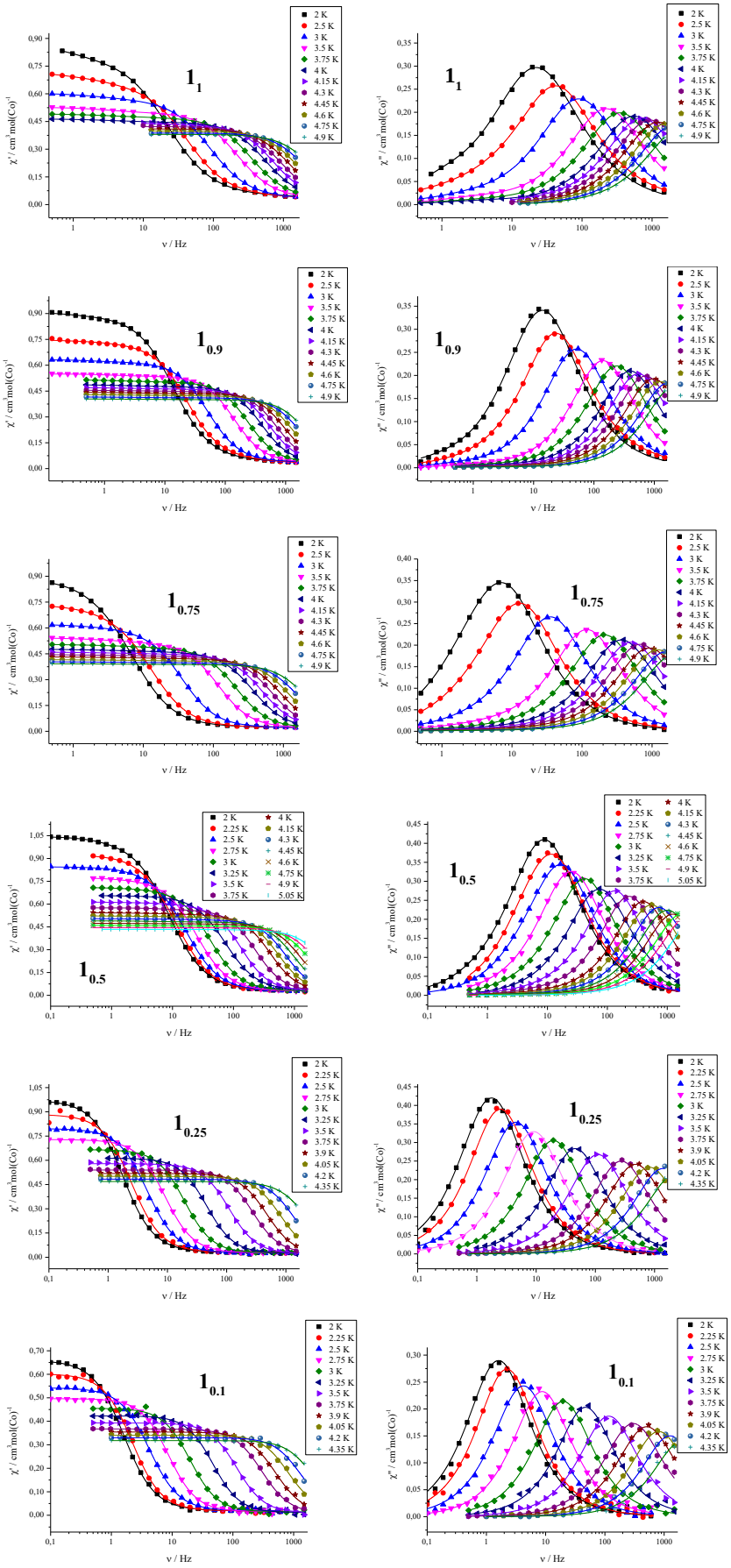

Figure S 31. In-phase χ' (left) and out-of-phase χ'' (right) components of AC magnetic susceptibility as function of frequency ν of ***1₁***, ***1₀.₉***, ***1₀.₇₅***, ***1₀.₅***, ***1₀.₂₅***, *and* ***1₀.₁*** *(from top to bottom) at the indicated temperatures and an applied DC field of 200 mT. Simultaneous fits of χ'(ν) and χ''(ν) with the generalized Debye model are shown as solid lines.*

Under an applied DC field of 200 mT clear χ" could be detected for all samples at all temperatures and for most temperatures even a clear maximum was observed. For further analysis we used the generalized Debye model to extract relaxation times τ,

$$\chi'(\nu) = \chi_0 + \sum_{n=1}^{N} (\chi_n - \chi_{n-1}) \frac{1 + (2\pi\nu\tau_n)^{1-\alpha_n} \sin(\pi\alpha_n/2)}{1 + 2(2\pi\nu\tau_n)^{1-\alpha_n} \sin(\pi\alpha_n/2) + (2\pi\nu\tau_n)^{2-2\alpha_n}}, \quad (S3)$$

$$\chi''(\nu) = \sum_{n=1}^{N} (\chi_n - \chi_{n-1}) \frac{(2\pi\nu\tau_n)^{1-\alpha_n} \cos\left(\frac{\pi\alpha_n}{2}\right)}{1 + 2(2\pi\nu\tau_n)^{1-\alpha_n} \sin\left(\frac{\pi\alpha_n}{2}\right) + (2\pi\nu\tau_n)^{2-2\alpha_n}}, \quad (S4)$$

with χ_0 the isothermal magnetic susceptibility. Equations S1 and S2 include N relaxation processes with corresponding adiabatic magnetic susceptibility χ_n, relaxation time τ_n and distribution parameter α_n. For **1$_{0.25}$** and **1$_{0.1}$** N = 1 was sufficient. In order to obtain excellent fits we used N = 2 for **1$_1$**, **1$_{0.9}$**, **1$_{0.75}$**, and **1$_{0.5}$**. While it significantly improved the fit quality, it turned out that the parameters for n = 2 could not be reliably obtained from our data. Therefore we will use only those for n = 1 for further analysis. The best-fit parameters are summarized in Table S7.

Table S7: Best-fit parameters to the generalized Debye model

relaxation times τ_1 (s):

T, K	**1$_1$**	**1$_{0.9}$**	**1$_{0.75}$**	*T*, K	**1$_{0.5}$**	*T*, K	**1$_{0.25}$**	**1$_{0.1}$**
2	0.00712	0.0113	0.0194	2	0.0180	2	0.0900	0.0992
2.5	0.00364	0.00687	0.0116	2.25	0.0125	2.25	0.0638	0.0718
3	0.00175	0.00307	0.00441	2.5	0.00923	2.5	0.0348	0.0377
3.5	7.14E-4	0.00113	0.00135	2.75	0.00640	2.75	0.0175	0.0182
3.75	4.55E-4	6.643E-4	7.50E-4	3	0.00373	3	0.00815	0.00805
4	2.89E-4	3.97E-4	4.33E-4	3.25	0.00215	3.25	0.00347	0.00337
4.15	2.23E-4	2.93E-4	3.18E-4	3.5	0.00117	3.5	0.00144	0.00137
4.3	1.70E-4	2.22E-4	2.33E-4	3.75	6.87E-4	3.75	5.83E-4	5.30E-4
4.45	1.30E-4	1.65E-4	1.75E-4	4	3.97E-4	3.9	3.34E-4	3.13E-4
4.6	1.03E-4	1.26E-4	1.32E-4	4.15	2.92E-4	4.05	1.95E-4	1.97E-4
4.75	7.89E-5	9.15E-5	9.97E-5	4.3	2.19E-4	4.2	1.13E-4	1.26E-4
4.9	6.13E-5	7.31E-5	7.62E-5	4.45	1.58E-4	4.35	6.75E-5	8.13E-5
				4.6	1.28E-4			
				4.75	8.61E-5			
				4.9	6.71E-5			
				5.05	5.27E-5			

α_1:

T, K	**1**$_1$	**1**$_{0.9}$	**1**$_{0.75}$	*T*, K	**1**$_{0.5}$	*T*, K	**1**$_{0.25}$	**1**$_{0.1}$
2	0.1676	0.1439	0.0970	2	0.1257	2	0.0758	0.0659
2.5	0.0777	0.0730	0.0771	2.25	0.1019	2.25	0.0601	0.0412
3	0.1077	0.0818	0.0441	2.5	0.0863	2.5	0.0527	0.0485
3.5	0.0787	0.0523	0.0284	2.75	0.0813	2.75	0.0408	0.0214
3.75	0.0651	0.0426	0.0201	3	0.0387	3	0.0298	0.0186
4	0.0530	0.0366	0.0229	3.25	0.0674	3.25	0.0248	0.0079
4.15	0.0410	0.0337	0.0138	3.5	0.0037	3.5	0.0277	0.0161
4.3	0,0349	0.0168	0.0076	3.75	0.0204	3.75	0.0210	0.0261
4.45	0.0419	0.0240	0.0122	4	0.0042	3.9	0.0270	0.0287
4.6	0.0241	0.0147	0	4.15	0.0092	4.05	0.0287	0
4.75	0.0299	0.0337	0	4.3	0.0052	4.2	0.0315	0
4.9	0.0270	0.0174	0.0123	4.45	0.0291	4.35	0.0463	0
				4.6	0			
				4.75	0.0357			
				4.9	0.0303			
				5.05	0			

χ_0 ($cm^3(mol\ Co)^{-1}$):

T, K	**1**$_1$	**1**$_{0.9}$	**1**$_{0.75}$	*T*, K	**1**$_{0.5}$	*T*, K	**1**$_{0.25}$	**1**$_{0.1}$
2	0.04026	0.03815	0.02276	2	0.02738	2	0.02805	0.01795
2.5	0.02228	0.02129	0.02143	2.25	0.02685	2.25	0.02861	0.01816
3	0.03260	0.03684	0.02119	2.5	0.02753	2.5	0.02613	0.01878
3.5	0.03097	0.03481	0.02066	2.75	0.02523	2.75	0.02660	0.01592
3.75	0.03135	0.03339	0.01923	3	0.02578	3	0.02611	0.01459
4	0.03088	0.03295	0.01834	3.25	0.03168	3.25	0.02397	0.01163
4.15	0.03251	0.03265	0.02042	3.5	0.02668	3.5	0.02029	0.01017
4.3	0.03282	0.03680	0.01966	3.75	0.02633	3.75	0.02323	0.00692
4.45	0.02991	0.03527	0.02403	4	0.02846	3.9	0.01540	0.00503
4.6	0.03426	0.03852	0.02178	4.15	0.02432	4.05	0.01228	0.02410
4.75	0.02810	0.02251	0.01034	4.3	0.02835	4.2	0	0.02990
4.9	0.02863	0.03488	0.02263	4.45	0.01548	4.35	0	0.03979
				4.6	0.03776			
				4.75	0			
				4.9	0			
				5.05	0.02313			

χ_1(cm^3(mol Co)$^{-1}$):

T, K	**1**$_1$	**1**$_{0.9}$	**1**$_{0.75}$	*T*, K	**1**$_{0.5}$	*T*, K	**1**$_{0.25}$	**1**$_{0.1}$
2	0.4707	0.8943	0.6826	2	1.0221	2	0.9741	0.6611
2.5	0.5095	0.6056	0.6275	2.25	0.8316	2.25	0.8853	0.6026
3	0.5715	0.6218	0.5709	2.5	0.7891	2.5	0.7968	0.5429
3.5	0.4997	0.5382	0.5089	2.75	0.7649	2.75	0.7288	0.4964
3.75	0.4707	0.5047	0.4730	3	0.6263	3	0.6664	0.4554
4	0.4468	0.4764	0.4544	3.25	0.6531	3.25	0.6137	0.4229
4.15	0.4327	0.4612	0.4395	3.5	0.5448	3.5	0.5792	0.3929
4.3	0.4200	0.4422	0.4231	3.75	0.5634	3.75	0.5399	0.3675
4.45	0.4082	0.4351	0.4154	4	0.5189	3.9	0.5186	0.3545
4.6	0.3971	0.4182	0.3952	4.15	0.5001	4.05	0.5006	0.3405
4.75	0.3869	0.4112	0.3743	4.3	0.4909	4.2	0.4834	0.3300
4.9	0.3780	0.3976	0.3849	4.45	0.4838	4.35	0.4689	0.3177
				4.6	0.4618			
				4.75	0.4570			
				4.9	0.4438			
				5.05	0.4182			

χ_2(cm^3(mol Co)$^{-1}$):

T, K	**1**$_1$	**1**$_{0.9}$	**1**$_{0.75}$	*T*, K	**1**$_{0.5}$
2	0.8634	0.9075	0.8889	2	1.0456
2.5	0.7401	0.7512	0.7392	2.25	0.9249
3	0.6052	0.6320	0.6233	2.5	0.8456
3.5	0.5271	0.5493	0.5438	2.75	0.7737
3.75	0.4920	0.5147	0.5070	3	0.7115
4	0.4640	0.4867	0.4786	3.25	0.6562
4.15	0.4423	0.4711	0.4626	3.5	0.6146
4.3	0.4256	0.4593	0.4472	3.75	0.5753
4.45	0.4099	0.4433	0.4339	4	0.5448
4.6	0.4086	0.4330	0.4191	4.15	0.5243
4.75	0.3876	0.4169	0.4082	4.3	0.5051
4.9	0.3804	0.4079	0.3940	4.45	0.4896
				4.6	0.4752
				4.75	0.4607
				4.9	0.4454
				5.05	0.4341

τ_2 (s):

T, K	$\mathbf{1}_1$	$\mathbf{1}_{0.9}$	$\mathbf{1}_{0.75}$	*T*, K	$\mathbf{1}_{0.5}$
2	0.159	0.637	0.064	2	0.207
2.5	0.013	0.005	0.048	2.25	0.038
3	0.068	0.271	0.032	2.5	0.048
3.5	0.053	0.127	0.037	2.75	0.111
3.75	0.045	0.080	0.014	3	0.006
4	0.045	0.064	0.021	3.25	0.020
4.15	0.008	0.057	0.016	3.5	0.003
4.3	0.0005	0.032	0.006	3.75	0.024
4.45	0.002	0.046	0.011	4	0.006
4.6	0.032	0.016	0.002	4.15	0.003
4.75	0.003	0.080	0.0002	4.3	0.005
4.9	0.002	0.064	0.016	4.45	0.035
				4.6	0.002
				4.75	0.048
				4.9	0.007
				5.05	0.0003

α_2:

T, K	$\mathbf{1}_1$	$\mathbf{1}_{0.9}$	$\mathbf{1}_{0.75}$	*T*, K	$\mathbf{1}_{0.5}$
2	0	0	0.13	2	0
2.5	0.52	0.5	0.21	2.25	0
3	0.19	0	0.29	2.5	0.05
3.5	0.12	0.04	0.27	2.75	0
3.75	0.24	0.06	0.42	3	0.3
4	0.17	0.13	0.4	3.25	0
4.15	0	0.2	0.5	3.5	0.3
4.3	0	0.6	0.5	3.75	0
4.45	0	0.2	0.5	4	0.4
4.6	0.2	0.6	0.7	4.15	0.6
4.75	0	0.3	0.8	4.3	0.5
4.9	0	0.7	0.6	4.45	0
				4.6	0.6
				4.75	0.2
				4.9	0.07
				5.05	0.3

The obtained temperature dependence of τ is shown in Figure 2 of the main text. In order to analyze it further we assumed that relaxation might happen via a direct, a Raman and an Orbach process.[9]

$$\frac{1}{\tau} = BT + CT^n + \frac{1}{\tau_0} e^{-\frac{U_{eff}}{k_B T}}, \qquad (S5)$$

where the first term, linear in the temperature T, models a direct process. The second term describes a Raman process, where the exponent n should be 9 for a Kramers ion like Co^{II}.[9] However, lower n are possible if both optical and acoustic phonons contribute.[9] The least-square fits were done to the data in the form of $\ln \tau$ as function of $1/T$. The fit results are summarized in Table S 8 and the fits are compared to the data in Figure S 32. For the HCM it was sufficient to include a direct and a Raman process. While for **1₁** the exponent n had to be included in the fit and n = 7.6 was obtained, excellent fits were obtained for **1$_{0.9}$**, **1$_{0.75}$**, and **1$_{0.5}$** with n fixed to 9. Including an Orbach process instead of the Raman process lead to reasonable fits, however the obtained U_{eff} were more than 3 times lower than the experimentally observed Δ. Hence, we could safely exclude this relaxation mechanism for HCM. For the LCM considering only a direct and a Raman process with fixed n = 9 gave poor results. Including n into the fit gave n of 12.5 to 13. Such high exponent seemed unreasonable to us. Leaving n = 9 fixed and including an Orbach process resulted in excellent fits with U_{eff} reasonably close to the experimentally observed Δ. Indeed, fixing U_{eff} to Δ lead to very similar fits. Presence of an Orbach process means presence of an energy barrier for thermal relaxation. Hence, we can conclude that the LCM have such a barrier.

Table S 8. Best-fit parameter for fits of equation S3 to $\ln \tau$ as function of $1/T$. Parameters highlighted in the table correspond to the solid line fit shown in Figure 2 of the main text.

Compound, comments		B, $s^{-1} \cdot K^{-1}$	$C \cdot 10^3$, $s^{-1} \cdot K^{-9}$	$1/\tau_0$, s^{-1}	U_{eff}, cm^{-1}
$\mathbf{1}_1$	Direct + Raman (n=9)	85 ± 8	11.2 ± 0.6 $s^{-1} \cdot K^{-9}$	–	–
	Direct + Raman (n=7.6)	66 ± 3	80 ± 10 $s^{-1} \cdot K^{-7.6}$	–	–
	Direct + Orbach	82 ± 7	–	$(8 \pm 3) \cdot 10^6$	21 ± 1
$\mathbf{1}_{0.9}$	Direct + Raman (n=9)	44 ± 1	8.8 ± 0.1	–	–
$\mathbf{1}_{0.75}$	Direct + Raman (n=9)	23.0 ± 0.5	8.23 ± 0.07	–	–
$\mathbf{1}_{0.5}$	Direct + Raman (n=9)	27.9 ± 0.8	9.1 ± 0.1	–	–
	Direct + Orbach	34 ± 2	–	$(1.7 \pm 0.4) \cdot 10^7$	24.4 ± 0.7
$\mathbf{1}_{0.25}$	Direct + Raman (n=9)	[1 ± 2]	11 ± 2	–	–
	Direct + Raman (n=9) + Orbach (U_{eff} is allowed to vary)	4.0 ± 0.2	5.0 ± 0.2	$(5 \pm 2) \cdot 10^{10}$	46 ± 1
	Direct + Raman (n=9) + Orbach (U_{eff} is fixed to Δ=49 cm^{-1})	3.9 ± 0.2	5.3 ± 0.2	$(1.37 \pm 0.04) \cdot 10^{11}$	49 (fixed)
$\mathbf{1}_{0.1}$	Direct + Raman (n=9)	[1 ± 2]	11 ± 2	–	–
	Direct + Raman (n=9) + Orbach (U_{eff} is allowed to vary)	3.8 ± 0.2	4.3 ± 0.2	$(5 \pm 2) \cdot 10^9$	39.8 ± 0.9
	Direct + Raman (n=9) + Orbach (U_{eff} is fixed to Δ=49 cm^{-1})	3.1 ± 0.4	5.6 ± 0.4	$(1.3 \pm 0.1) \cdot 10^{11}$	49 (fixed)

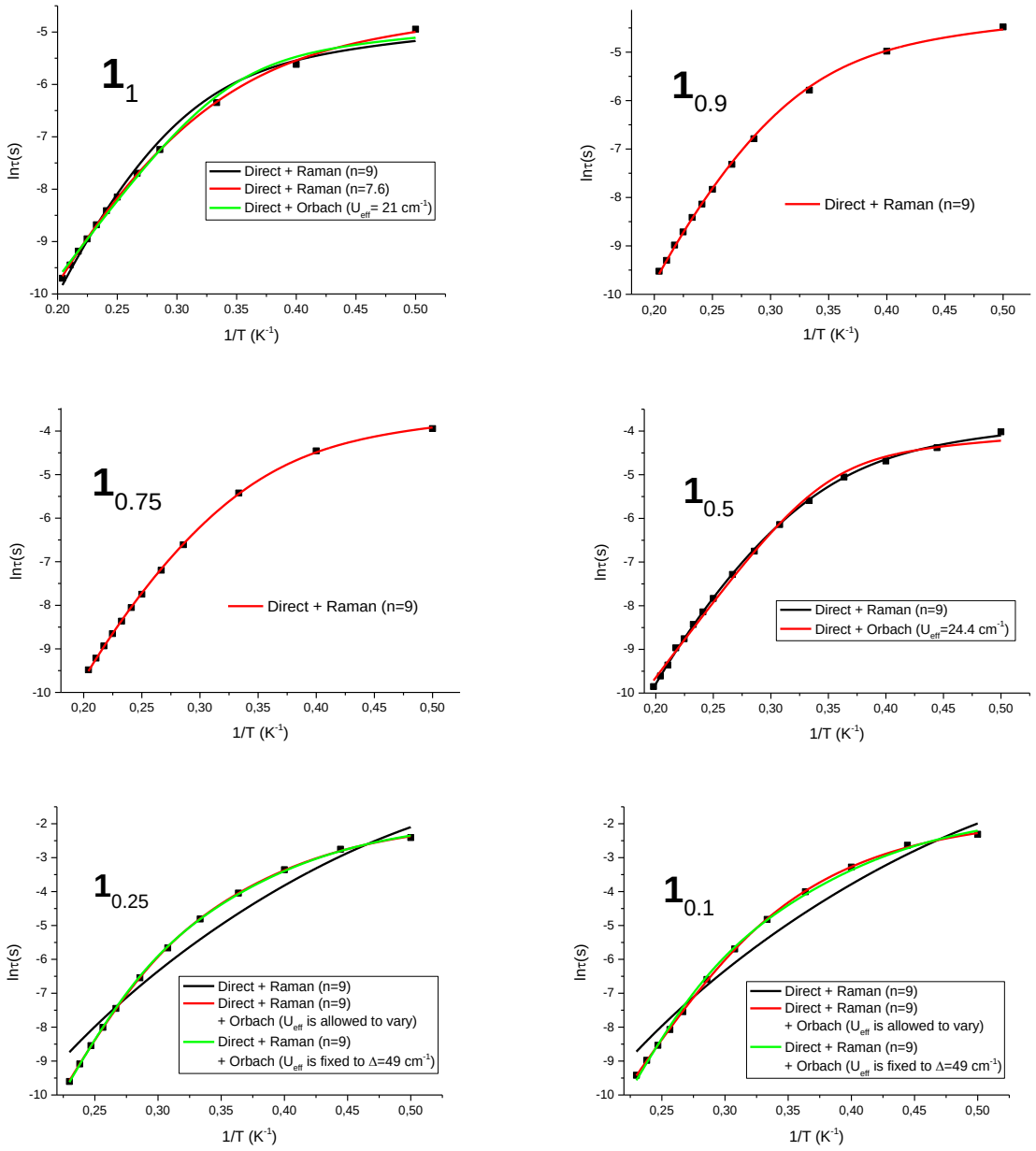

Figure S 32. Relaxation times shown as $ln\,\tau$ vs. $1/T$. Lines correspond to fits with equation S3 and the parameters given in Table S 8.

5. Ab initio Calculations

10 quartet and 40 doublet states of the Co(II) complexes have been calculated using the CASSCF(7,5)/NEVPT2 method with DKH-def2-TZVP basis set with ORCA 4.1.1. Molecular structures were taken from X-Ray data without geometry optimization. Two enantiomers are present in the crystal, for a sake of consistency we have chosen the same type of enantiomers for all calculations. Irrespective of the Co/Zn ratio always a Co(II) molecule was calculated, therefore $\mathbf{1_0}$ corresponds to a fictitious Co(II) molecule in the pure Zn(II) matrix. Results of calculations for all available X-Ray structures show only subtle differences inside the HCM and LCM groups.

Table S 9. Calculated ZFS and spin Hamiltonian parameters D and E as obtained from the effective Hamiltonian in comparison with the experimentally observed ZFS.

	Δ, cm^{-1}	D, cm^{-1}	E/D	Experimental Δ, cm^{-1}
$\mathbf{1_0}$	42.69	-21.01	0.103	-
$\mathbf{1_{0.1}}$	44.18	-21.80	0.094	49
$\mathbf{1_{0.25}}$	45.58	-22.48	0.096	
$\mathbf{1_{0.5}}$	76.45	37.80	0.087	75
$\mathbf{1_{0.75}}$	77.30	38.45	0.058	
$\mathbf{1_{0.9}}$	78.28	39.04	0.041	
$\mathbf{1_1}$	82.00	40.95	0.030	

The calculated Δ are rather close to the experimentally observed ones (see Table S 9). However, an important difference should be noted. While experimentally, Δ was observed as almost identical within the HCM and LCM series, the calculated Δ is different for each molecule. The calculated trend in Δ can be directly linked to differences in bond length between the metal center and the atoms in the first ligation shell (see Figure S 33). The correlation is particularly striking for the ligating oxygen atoms. The correlation is less obvious for N, however, the differences in bond lengths were also much smaller. It was not possible to draw similar conclusions for the bond angles. The calculated differences clearly exceed the experimental resolution and uncertainty (better than 1 cm^{-1}). However, experimentally Δ was 75 cm^{-1} for all HCM and 49 cm^{-1} for LCM. The molecular structure refined from X-Ray diffraction spectra are an average over all molecules within the crystal. Hence, one might argue that the perceived differences in bond lengths inside the HCM and LCM groups are rather a result of averaging bond lengths. This would mean the HCM would be a mixture of $\mathbf{1_1}$ with a Zn-containing molecule structurally very close to, but not identical to, $\mathbf{1_1}$. Similarly for LCM a Co-containing molecule that is structurally very close to $\mathbf{1_0}$ would be mixed with $\mathbf{1_0}$. Given that Δ is usually extremely sensitive to small changes of the bond length[10] and the explanation is in line with XRD results this seems likely to be the case. However, we would like to stress that although trends in Δ are often astonishingly well reproduced by CASSCF/NEVPT2 calculations an overall agreement with experiment within 20 % is currently considered as good match.[11] The calculated differences are well below that and in fact all calculated values of Δ fall within this threshold.

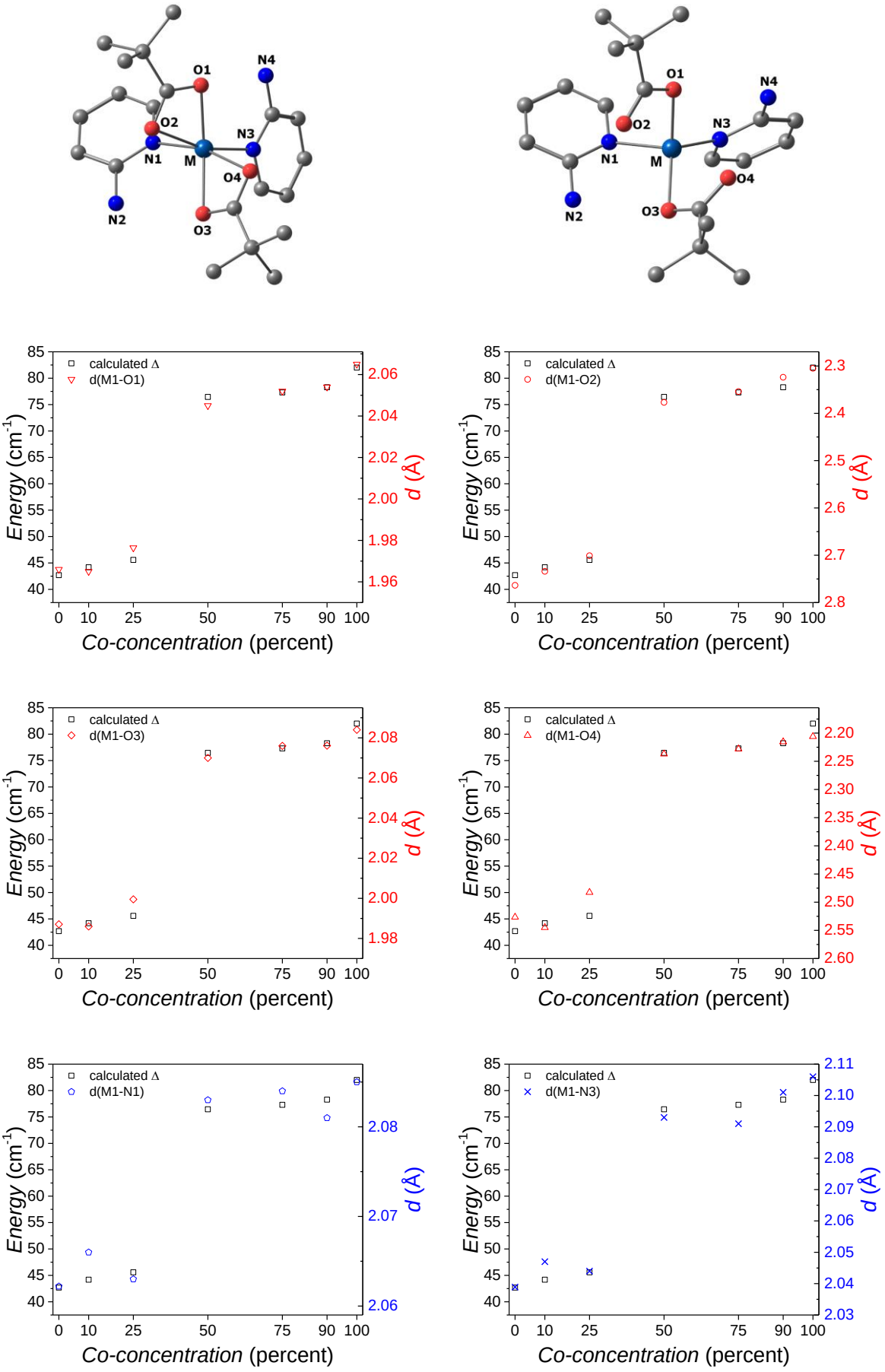

Figure S 33. Calculated Δ (black squares and left y scale) compared to metal-ligand bond length (right y scale) for the first ligation shell. Each plot shows one particular bond length. For simpler identification of the respective bonds the structure of the molecules ***1₁*** (left) *and* ***1₀*** *(right) are shown on the top in ball-and-stick representation. Metal ion: teal, O: red, N: blue, C: gray, H and counterion omitted.*

Table S 10. Calculated and experimental g-factors of the S = 3/2 model and the effective g'-factors of the lowest Kramers doublets.

	Calculated						Experimental					
	g_1	g_2	g_3	g'_1	g'_2	g'_3	g_1	g_2	g_3	g'_1	g'_2	g'_3
1_0	2.1514	2.1911	2.3988	0.6194	0.7063	7.1143	-		-	-	-	-
$1_{0.01}$	-	-	-	-	-	-	2.25		2.38	0.93	0.79	7.03
$1_{0.1}$	2.1508	2.1919	2.4054	0.5674	0.6415	7.1470	2.25		2.38	0.82	0.93	6.85
$1_{0.25}$	2.1498	2.1948	2.4155	0.5820	0.6587	7.1727	2.25		2.44	0.87	0.87	7.15
$1_{0.5}$	2.0912	2.4620	2.4901	2.0954	4.2182	5.5959	2.21		2.53	2.11	4.09	5.89
$1_{0.75}$	2.0903	2.4754	2.4815	2.1237	4.4612	5.3849	2.17		2.43	2.10	4.08	5.57
$1_{0.9}$	2.0882	2.4746	2.4862	2.1353	4.6078	5.2553	2.23		2.65	2.10	4.30	5.94
1_1	2.0858	2.4618	2.5236	2.1473	4.7025	5.2163	2.21		2.54	2.11	4.11	5.88

In contrast to the calculated D and E the calculated Δ does not rely on the validity of a spin Hamiltonian approach.

The effective g' tensor of the ground state doublet is a good indicator for the type of anisotropy. EPR experiments with $h\nu \ll \Delta$ and $k_B T \ll \Delta$ allow to experimentally determine the principal values of those effective g'.[13] These conditions are fulfilled for the here studied molecules. Corresponding experimental spectra are shown in section 3 of the SI (Figure S 25 and Table S 5) and the calculated values are summarized in Table S 10. Easy-axis type of anisotropy is characterized by one high (typically 7 or higher) and two low (1 or even lower) principal values. The main magnetic axis, i.e. the easy-axis corresponds to the axis of the largest principal value of the effective g' tensor.[14] The combination of large and small principal values of the effective g' tensor provides an experimental challenge. To the contrary, the observation of an X-Band EPR spectrum for Co^{II} with easy-plane type of anisotropy is straightforward. The principal values span a range of around 6 to 2 and the axis corresponding to the smallest principal value is the main magnetic axis, i.e. the hard axis. The principal values of the calculated effective g' tensors are compared to experimental results in Table S 10. Qualitatively they agree with the experimental results, identifying easy-plane type of anisotropy for HCM and easy-axis type for LCM. The effective g'-tensors are shown for structures **1_1** and **1_0** in Figure S 34. In the case of **1_1** the tensor is oblate, and the smallest component almost coincides with the pseudo C_2 axis (pointing out of the Figure S 34). In the case of **1_0**, the tensor is prolate, and the main component almost perpendicular to the pseudo C_2 axis (~107° with respect to the axis that links M and the middle of O1 and O3).

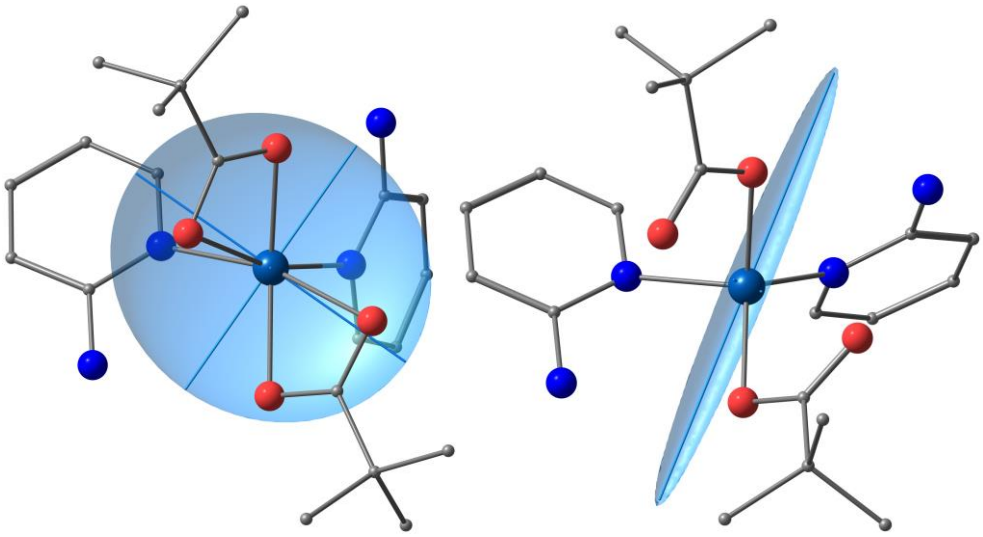

*Figure S 34. X-Ray structure of **1₁** (left) and **1₀** (right) orientated so that the pseudo-C_2 symmetry axis is pointing out-of-plane of the figure; effective g'-tensor and its components are represented as light blue ellipsoids and vectors, which lengths correspond to the eigenvalues. Co: teal, O: red, N: blue, C: gray, H atoms are omited.*

In the following we discuss the results of **1₁** and **1₀** as examples for HCM and LCM in more details.

The energies of the non-relativistic states are different for **1₁** and **1₀** (Table S 11). Spin-orbit coupling was taken into account via the mean-field approximation, and individual contributions to the ZFS parameters from each excited state reveal the difference in the nature of the ground and excited states for the two molecular structures. For **1₁** the largest contribution to D comes from the two lowest lying excited states, which are close in energy. Both of them contribute positively to D and the overall D is positive as well. In contrast for **1₀** the dominant contribution is from a single state and negative, as well as the overall D. However, it should be noted that the contributions of the individual states to D are calculated in a perturbative manner. In contrast, the actual D is calculated in the effective Hamiltonian approach.[15,16] Hence the contributions don't add up to the actual D, and should be considered as an estimate for guidance.

Table S 11.Non-relativistic relative energies of the excited states and their individual contribution to ZFS parameters D and E of the ground quartet state.

1_0				**1_1**			
$2S+1$	Energy, cm^{-1}	D, cm^{-1}	E, cm^{-1}	$2S+1$	Energy, cm^{-1}	D, cm^{-1}	E, cm^{-1}
4	**3043**	**-29.0**	**0.6**	**4**	**1362**	**24.4**	**9.0**
4	5399	3.9	-1.8	**4**	**1647**	**19.0**	**-4.8**
4	6932	6.9	0.5	4	8025	-7.6	-1.7
4	7724	-2.0	-1.0	4	8374	-1.3	-0.9
4	9686	-0.3	-0.1	4	9071	0.8	-0.3
4	13408	0.0	0.0	2	11598	0.2	0.0
2	15654	-1.0	0.1	2	12794	-1.2	-1.4
2	17184	-0.4	-0.3	4	16915	0.0	0.0
2	18414	0.0	0.0	2	18309	0.0	0.0
2	19229	0.2	-0.1	2	18757	0.0	0.0
4	19877	0.0	0.0	2	19279	-0.6	0.2
2	20041	0.1	0.0	2	19440	-0.8	-0.4
2	20777	0.0	0.0	2	19757	-0.7	-0.6
2	21594	3.3	-0.1	2	19998	-0.7	0.6
2	22682	-2.0	0.5	4	21683	0.0	0.0
4	22971	0.0	0.0	4	21987	0.0	0.0
4	23355	0.0	0.0	2	22941	-0.2	0.0
2	23493	0.7	0.1	2	23027	0.0	0.0
2	23962	-2.4	-1.2	4	23170	0.0	0.0
2	25070	0.0	0.0	2	23316	-0.1	0.1
2	25137	0.1	0.0	2	25041	3.3	0.0
2	26632	0.1	0.0	2	27326	0.0	-0.1
2	27061	-0.1	0.1	2	27804	0.0	0.1
2	27332	-0.1	-0.1	2	28770	-0.2	0.3
2	28196	-0.1	0.3	2	28777	-0.3	0.0
2	28296	0.0	0.0	2	29029	-0.1	-0.1
2	29633	-0.1	-0.1	2	29543	-0.1	0.1
2	29839	0.1	0.0	2	31080	-0.4	-0.3
2	30152	0.0	0.1	2	31442	0.1	-0.1
2	30669	-0.1	0.0	2	32939	1.3	0.0
2	31734	0.0	0.0	2	33598	-0.1	-0.1
2	31885	-0.4	-0.2	2	34103	-0.2	0.2
2	32216	-0.6	0.2	2	34669	-0.2	0.2
2	33623	0.0	0.0	2	34722	0.0	-0.1
2	34300	0.5	0.0	2	35368	-0.1	-0.1
2	35090	0.0	0.0	2	35564	0.0	0.0
2	36156	0.0	0.0	2	35949	0.0	0.0
2	41689	0.0	0.0	2	42143	-0.1	0.1
2	42073	0.1	0.0	2	42554	0.2	0.0
2	42572	0.1	0.0	2	42954	0.0	0.0
2	43394	-0.1	0.0	2	43785	0.0	0.0
2	43993	0.0	0.0	2	44088	-0.1	0.0
2	44337	0.0	0.0	2	44729	0.0	0.0
2	44842	0.0	0.0	2	45056	0.0	0.0
2	62058	0.0	0.0	2	64050	0.0	0.0
2	62476	0.0	0.0	2	64385	0.0	0.0
2	63948	0.0	0.0	2	65053	0.0	0.0
2	64940	0.0	0.0	2	65264	0.0	0.0
2	66275	0.0	0.0	2	65853	0.0	0.0

Based on the energies and the wavefunctions of 10 quartet and 40 doublet states the ligand field theory parameters of the interelectronic repulsion B and C (Racah parameters) and *d*-orbitals splitting and mixing (5-by-5 LFT matrix) were extracted as implemented in the AILFT module in ORCA. The AILFT *d*-orbital splitting shows a dramatic change due to structural differences between $\mathbf{1_1}$ and $\mathbf{1_0}$.

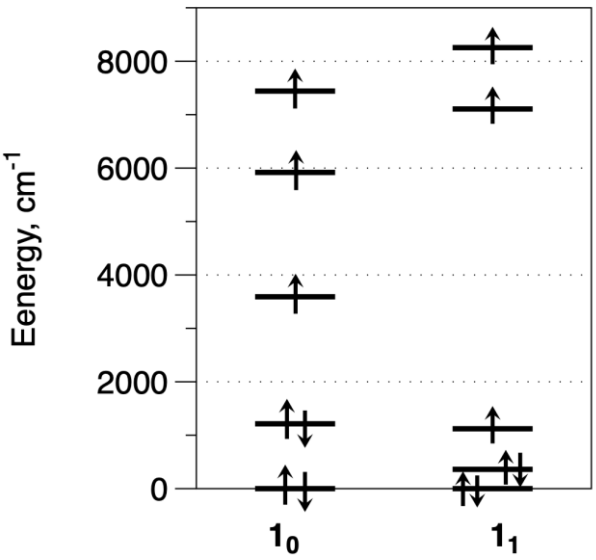

Figure S 35. AILFT d-orbitals splitting computed with CASSCF(7,5)/NEVPT2. For $\mathbf{1_0}$*, the splitting resembles a distorted terahedral enviroment, while* $\mathbf{1_1}$ *show an almost octahedral splitting. The corresponding orbitals are shown in Table S 12.*

The shape of the AILFT orbitals (see Table S 12 and Table S 13) reflects the differences in the coordination environment. $\mathbf{1_0}$ is characterized by a wider N-M-N angle and smaller O-M-O angle compared to $\mathbf{1_1}$ (see Table S 2**)**. At the given electronic configuration, the lowest energy one-electron excitation is from the second d-orbital to the third one (2-> 3). Markedly the symmetry of those orbitals is quite different for $\mathbf{1_1}$ and $\mathbf{1_0}$**.** The contributions to *D* from the lowest excited states have opposite sign. Unfortunately, in both cases the symmetry is very low, inhibiting a further analysis.

Table S 12. AILFT d*-orbitals isosurfaces for* ***1₀*** *and* ***1₁****, which correspond to the energy diagram in Figure S 35 and coefficients in Table S 13.*

	1_0	1_1
5	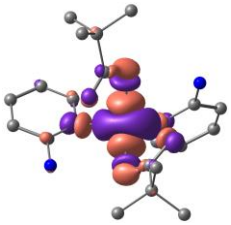	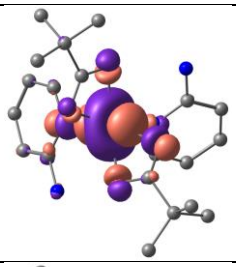
4	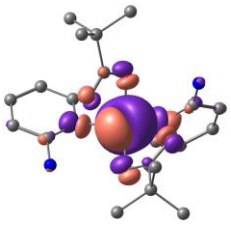	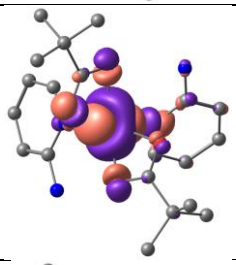
3	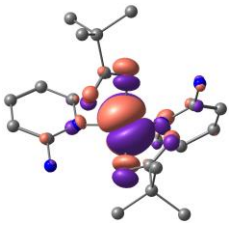	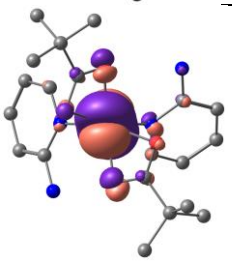
2	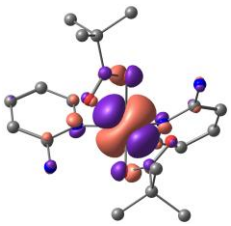	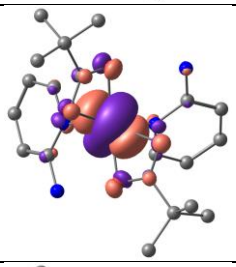
1	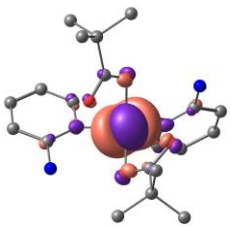	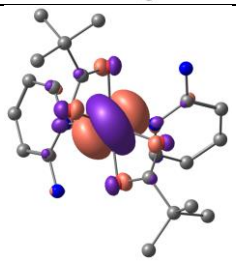

Table S 13. AILFT parameters computed with CASSCF(7,5)/NEVPT2. Racah parameters B and C, relative energies of the d-orbitals and their wavefunctions defined in the X-Ray structure frames.

	1_0	**1_1**
B / cm^{-1}	1008.5	1030.2
C / cm^{-1}	3960.3	3982.7
ζ_{SOC} /cm^{-1}	514.3	518.7
Orbital 1		
Energy / eV	0	0
Energy / cm^{-1}	0	0
Coefficient d_{xy}	0.064186	0.46339
Coefficient d_{yz}	-0.07028	-0.40308
Coefficient d_{z2}	0.752195	-0.58024
Coefficient d_{xz}	-0.21651	-0.16474
Coefficient d_{x2-y2}	0.61533	-0.50889
Orbital 2		
Energy / eV	0.15	0.045
Energy / cm^{-1}	1213.6	361.2
Coefficient d_{xy}	-0.015314	0.003035
Coefficient d_{yz}	0.15961	-0.27171
Coefficient d_{z2}	0.65084	-0.50085
Coefficient d_{xz}	0.36031	-0.08687
Coefficient d_{x2-y2}	-0.64875	0.81717
Orbital 3		
Energy / eV	0.445	0.139
Energy / cm^{-1}	3591.2	1120.6
Coefficient d_{xy}	0.96962	-0.02608
Coefficient d_{yz}	0.2147	-0.73353
Coefficient d_{z2}	-0.039457	0.30854
Coefficient d_{xz}	-0.092129	0.60495
Coefficient d_{x2-y2}	-0.06082	0.009614
Orbital 4		
Energy / eV	0.734	0.881
Energy / cm^{-1}	5918.6	7106.3
Coefficient d_{xy}	0.19457	0.74994
Coefficient d_{yz}	-0.95373	0.39266
Coefficient d_{z2}	0.054544	0.017449
Coefficient d_{xz}	-0.055834	0.49651
Coefficient d_{x2-y2}	-0.21553	0.19125
Orbital 5		
Energy / eV	0.923	1.023
Energy / cm^{-1}	7441.3	8254.9
Coefficient d_{xy}	0.13276	0.47134
Coefficient d_{yz}	-0.11787	-0.26731
Coefficient d_{z2}	-0.080238	0.563
Coefficient d_{xz}	0.90094	-0.59399
Coefficient d_{x2-y2}	0.38775	0.19129

In an attempt to rationalize the fundamental structural differences between $\mathbf{1_1}$ and $\mathbf{1_0}$, we performed gas phase geometry optimization. They were performed with both Co and Zn as metal ion. We optimized $\mathbf{1_0(Co)}$, and $\mathbf{1_0(Zn)}$, i.e. starting from the molecular structure of $\mathbf{1_0}$ as refined from X-Ray diffraction, with the metal ion being Co and Zn, respectively. The B3LYP/def2SVP method was used and harmonic frequency calculations confirmed the minimal energy structures. Optimized gas phase structures quite similar 6-coordinate complexes with M-O bonds ranging from 2.11 to 2.22 Å similar to $\mathbf{1_1}$ (see Table S 14). However, a slight difference was observed. If one writes the metal-oxygen bond distances as (M-O1, M-O2, M-O3, M-O4) one obtains (2.123, 2.243, 2.136, 2.227) Å, i.e. short-long-short-long, for $\mathbf{1_0(Zn)}$ and (2.110, 2.211, 2.219, 2.137) Å, corresponding to short-long-long-short for $\mathbf{1_0(Co)}$.

Table S 14. Optimized (B3LYP/def2-SVP) structure of ***1₁(Co)***, ***1₁(Zn)***, ***1₀(Co)***, *and* ***1₀(Zn),*** *starting from* ***1₁*** *and* ***1₀*** *X-Ray structures.*

Optimized structure of **1_0(Zn)**	Optimized structure of **1_0(Co)**
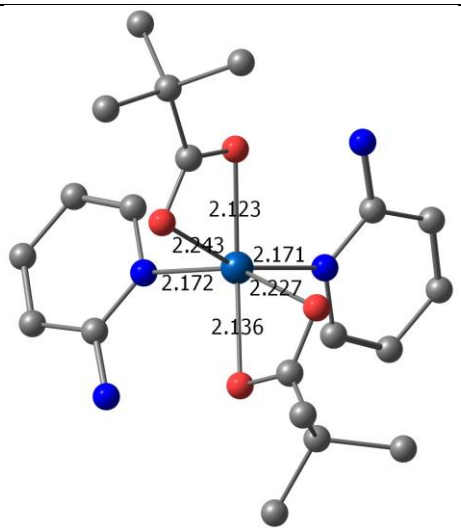	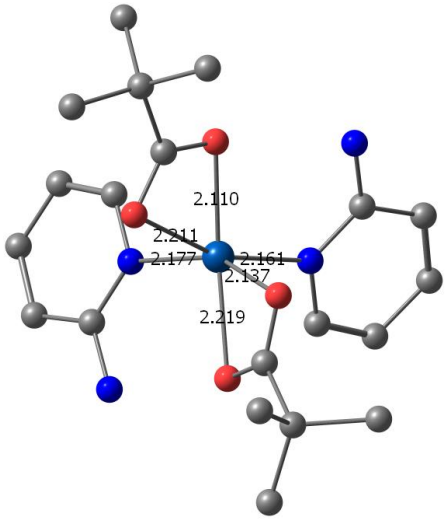
X-Ray structure of **1_0**	X-Ray structure of **1_1**
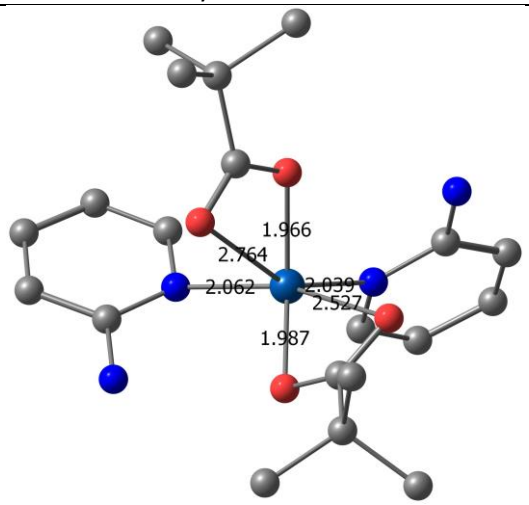	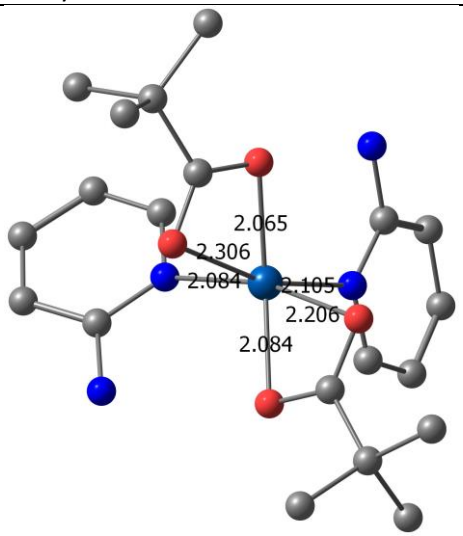

Optimized structure of $\mathbf{1_0(Zn)}$			
Zn	-0.002075000000	0.008539000000	-0.011942000000
O	-1.652619000000	-0.505479000000	1.220734000000
O	-1.411537000000	-1.612258000000	-0.657701000000
O	1.669095000000	-0.409055000000	-1.275180000000
O	1.440627000000	-1.588512000000	0.559154000000
N	0.925597000000	1.471300000000	1.296454000000
N	-0.393581000000	1.009748000000	3.158299000000
N	-0.970475000000	1.488965000000	-1.272566000000
N	0.343858000000	1.123108000000	-3.159373000000
C	-2.015268000000	-1.444302000000	0.419964000000
C	-3.187745000000	-2.345952000000	0.836633000000
C	-2.736240000000	-3.149823000000	2.075232000000
C	-3.555757000000	-3.301347000000	-0.307133000000
C	-4.393104000000	-1.458257000000	1.203779000000
C	2.049508000000	-1.364281000000	-0.508307000000
C	3.263198000000	-2.226128000000	-0.894447000000
C	2.804761000000	-3.698701000000	-0.920843000000
C	4.334552000000	-2.038183000000	0.200371000000
C	3.824757000000	-1.817898000000	-2.263448000000
C	1.944057000000	2.146632000000	0.727824000000
C	2.730965000000	3.064466000000	1.404072000000
C	2.445064000000	3.289443000000	2.762491000000
C	1.407874000000	2.605577000000	3.366247000000
C	0.638510000000	1.681702000000	2.604335000000
C	-2.001036000000	2.119362000000	-0.674686000000
C	-2.816794000000	3.038077000000	-1.314534000000
C	-2.548479000000	3.314161000000	-2.667074000000
C	-1.499224000000	2.677266000000	-3.300524000000
C	-0.699928000000	1.749455000000	-2.574994000000
H	-0.586443000000	1.127259000000	4.141919000000
H	-0.940180000000	0.334538000000	2.612823000000
H	0.915843000000	0.449180000000	-2.640176000000
H	0.527165000000	1.279952000000	-4.139293000000
H	-2.470119000000	-2.479580000000	2.906086000000
H	-1.856270000000	-3.771212000000	1.844656000000
H	-3.546620000000	-3.816963000000	2.412628000000
H	-3.864529000000	-2.745757000000	-1.205537000000
H	-4.386908000000	-3.958737000000	-0.002867000000
H	-2.698042000000	-3.928376000000	-0.589940000000
H	-4.730704000000	-0.866409000000	0.337222000000
H	-4.135123000000	-0.759421000000	2.012683000000
H	-5.239732000000	-2.081256000000	1.536323000000
H	2.383949000000	-3.990278000000	0.051952000000
H	3.655923000000	-4.360262000000	-1.152093000000
H	2.029450000000	-3.860367000000	-1.687105000000
H	3.931496000000	-2.308081000000	1.187220000000
H	4.679032000000	-0.991922000000	0.246536000000
H	5.210820000000	-2.673773000000	-0.008609000000
H	4.136999000000	-0.762794000000	-2.269531000000
H	3.073191000000	-1.946878000000	-3.057200000000
H	4.699924000000	-2.438820000000	-2.516580000000
H	2.130050000000	1.910282000000	-0.323603000000

Optimized structure of $\mathbf{1_0(Co)}$			
Co	-0.044710000000	0.012051000000	0.003134000000
O	-1.664408000000	-0.518988000000	1.246047000000
O	-1.634155000000	-1.298783000000	-0.799304000000
O	1.714393000000	-0.301073000000	-1.312002000000
O	1.122899000000	-1.766719000000	0.203171000000
N	1.118123000000	1.237165000000	1.350871000000
N	0.001570000000	0.472943000000	3.248278000000
N	-0.944772000000	1.664642000000	-1.091891000000
N	0.558210000000	1.665733000000	-2.871076000000
C	-2.152024000000	-1.287381000000	0.335580000000
C	-3.345918000000	-2.184534000000	0.691015000000
C	-2.843703000000	-3.232998000000	1.707941000000
C	-3.877849000000	-2.882789000000	-0.568329000000
C	-4.448164000000	-1.321302000000	1.334983000000
C	1.890353000000	-1.420925000000	-0.731642000000
C	3.034313000000	-2.355220000000	-1.155280000000
C	2.410402000000	-3.700364000000	-1.581665000000
C	3.942290000000	-2.572767000000	0.073302000000
C	3.839740000000	-1.749090000000	-2.312682000000
C	2.082374000000	1.999451000000	0.795826000000
C	2.956465000000	2.787328000000	1.526664000000
C	2.825934000000	2.779533000000	2.926765000000
C	1.844960000000	2.007332000000	3.517395000000
C	0.977024000000	1.229682000000	2.700327000000
C	-2.038537000000	2.177088000000	-0.492297000000
C	-2.794727000000	3.211483000000	-1.020299000000
C	-2.395381000000	3.743462000000	-2.258265000000
C	-1.280534000000	3.230814000000	-2.893333000000
C	-0.549588000000	2.173196000000	-2.284578000000
H	-0.118788000000	0.475723000000	4.250261000000
H	-0.675174000000	-0.027752000000	2.664273000000
H	1.046371000000	0.860382000000	-2.466133000000
H	0.820208000000	1.991704000000	-3.789731000000
H	-2.461435000000	-2.748501000000	2.618798000000
H	-2.030950000000	-3.841081000000	1.280077000000
H	-3.665195000000	-3.910676000000	1.993330000000
H	-4.224692000000	-2.150622000000	-1.313377000000
H	-4.723405000000	-3.541556000000	-0.310495000000
H	-3.094164000000	-3.488342000000	-1.045636000000
H	-4.822564000000	-0.561569000000	0.629298000000
H	-4.069521000000	-0.800400000000	2.226370000000
H	-5.301676000000	-1.951542000000	1.634369000000
H	1.814245000000	-4.128420000000	-0.763132000000
H	3.200849000000	-4.418075000000	-1.856781000000
H	1.747924000000	-3.573671000000	-2.453226000000
H	3.365860000000	-2.985308000000	0.913887000000
H	4.398863000000	-1.625584000000	0.404450000000
H	4.757121000000	-3.273454000000	-0.172757000000
H	4.270864000000	-0.776094000000	-2.033040000000
H	3.206506000000	-1.588637000000	-3.198437000000
H	4.663632000000	-2.423865000000	-2.597695000000
H	2.148850000000	1.946857000000	-0.293115000000

H	3.543456000000	3.581585000000	0.892461000000	H	3.718165000000	3.382999000000	1.022294000000
H	3.038637000000	4.000248000000	3.343765000000	H	3.494111000000	3.380141000000	3.549899000000
H	1.165356000000	2.761547000000	4.419781000000	H	1.719949000000	1.984340000000	4.602267000000
H	-2.172359000000	1.844809000000	0.369834000000	H	-2.306630000000	1.711791000000	0.460469000000
H	-3.637822000000	3.517101000000	-0.779991000000	H	-3.669564000000	3.585275000000	-0.487047000000
H	-3.164968000000	4.027771000000	-3.220392000000	H	-2.960584000000	4.556334000000	-2.722152000000
H	-1.269549000000	2.873431000000	-4.350211000000	H	-0.948338000000	3.623352000000	-3.857043000000

References

1. Fomina, I. G. *et al.* High-spin carboxylate polymers [M(OOCCMe3)2] n of group VIII 3d metals. *Russ. Chem. Bull.* **55**, 1909–1919 (2006).

2. Bokach, N. A. *et al.* Co(II)-mediated and microwave assisted coupling between 2,6-diaminopyridine and nitriles. A new synthetic route to N-(6-aminopyridin-2-yl)carboximidamides. *Russ. Chem. Bull. (Translation Izv. Akad. Nauk. Seriya Khimicheskaya)* **55**, 36–43 (2006).

3. SMART (Control) and SAINT (Integration). (1997).

4. Sheldrick, G. M. SADABS, Program for Scaling and Correction of Area Detector Data. (1997).

5. Sheldrick, G. M. A short history of SHELX. *Acta Crystallogr. Sect. A Found. Crystallogr.* **64**, 112–122 (2008).

6. Alvarez, S., Avnir, D., Llunell, M. & Pinsky, M. Continuous symmetry maps and shape classification. The case of six-coordinated metal compounds. *New J. Chem.* **26**, 996–1009 (2002).

7. Cirera, J., Alemany, P. & Alvarez, S. Mapping the Stereochemistry and Symmetry of Tetracoordinate Transition-Metal Complexes. *Chem. - A Eur. J.* **10**, 190–207 (2004).

8. Stoll, S. & Schweiger, A. EasySpin, a comprehensive software package for spectral simulation and analysis in EPR. *J. Magn. Reson.* **178**, 42–55 (2006).

9. Shrivastava, K. N. Theory of Spin–Lattice Relaxation. *Phys. status solidi* **117**, 437–458 (1983).

10. Suturina, E. A. *et al.* Magneto-Structural Correlations in Pseudotetrahedral Forms of the [Co(SPh)4]2– Complex Probed by Magnetometry, MCD Spectroscopy, Advanced EPR Techniques, and ab Initio Electronic Structure Calculations. *Inorg. Chem.* **56**, 3102–3118 (2017).

11. Atanasov, M. *et al.* First principles approach to the electronic structure, magnetic anisotropy and spin relaxation in mononuclear 3d-transition metal single molecule magnets. *Coord. Chem. Rev.* **289**, 177–214 (2015).

12. Atanasov, M., Ganyushin, D., Pantazis, D. A., Sivalingam, K. & Neese, F. Detailed Ab initio first-principles study of the magnetic anisotropy in a family of trigonal pyramidal iron(II) pyrrolide complexes. *Inorg. Chem.* **50**, 7460–7477 (2011).

13. Pilbrow, J. R. *Transition Ion Electron Paramagnetic Resonance*. (Clarendon Press, 1990).

14. Pilbrow, J. R. Effective G-Values for S = 3/2 and S = 5/2. *J. Magn. Reson.* **31**, 479–490 (1978).

15. Malrieu, J. P., Durand, P. & Daudey, J. P. Intermediate Hamiltonians as a new class of effective Hamiltonians. *J. Phys. A. Math. Gen.* **18**, 809–826 (1985).

16. Ganyushin, D. & Neese, F. First-principles calculations of zero-field splitting parameters. *J. Chem. Phys.* **125**, 024103 (2006).